ORNL/TM-2022/2618
CRADA/NFE-19-07933

Lithium-Ion Batteries with Safer Current Collectors

Jianlin Li
Hsin Wang
Srikanth Allu
Srdjan Simunovic
Kelsey Livingston
Nancy Dudney
et al.

October 2022

FINAL CRADA REPORT (CRADA/NFE-19-07933)

OAK RIDGE National Laboratory

ORNL IS MANAGED BY UT-BATTELLE LLC FOR THE US DEPARTMENT OF ENERGY

ORNL/TM-2022/2618
CRADA/NFE-19-07933

US Department of Energy
Office of Energy Efficiency and Renewable Energy
Technology Commercialization Fund Program

LITHIUM-ION BATTERIES WITH SAFER CURRENT COLLECTOR

Jianlin Li[1]
Hsin Wang[1]
Srikanth Allu[1]
Srdjan Simunovic[1]
Kelsey Livingston[1]
Nancy Dudney[1]
Brian Morin[2]
Carl Hu[2]
Drew Pereira[2]
Amy Brinson[2]

[1]Oak Ridge National Laboratory
[2]Soteria Battery Innovation Group

October 2022

Prepared by
OAK RIDGE NATIONAL LABORATORY
Oak Ridge, TN 37831
managed by
UT-BATTELLE LLC
for the
US DEPARTMENT OF ENERGY
under contract DE-AC05-00OR22725

CONTENTS

LIST OF FIGURES

LIST OF TABLES

ACKNOWLEDGMENTS

This work described in this report under CRADA NFE-19-07933 has been funded by the Technology Commercialization Fund Program of Office of Energy Efficiency & Renewable Energy within the US Department of Energy and Soteria Battery Innovation Group. The authors thank the R&D team, namely Jianlin Li, Hsin Wang, Srikanth Allu, Srdjan Simunovic, Kelsey Livingston, and Nancy Dudney at Oak Ridge National Laboratory, and Brian Morin, Carl Hu, Drew Pereira, and Amy Brinson at Soteria Battery Innovation Group, for their invaluable technical contributions making this project successful.

The authors are grateful for the local program support by Michael Paulus, Andrea Bowers, Sue Burchfield, Ronald Ott, Marc Filigenzi, Deb McCleary, Mark Reeves, Tammy Graham, Jennifer Caldwell, and Samuel Gillard at the Vehicle Technologies Office, and Steve Palmeri and David Yarwood at the Office of Technology Transition.

ABBREVIATIONS

BMF	Battery Manufacturing Facility
CRADA	Cooperative Research and Development Agreement
DOE	US Department of Energy
EUCAR	European Council for Automotive R&D
FE	finite element
LFP	lithium iron phosphate
LIB	lithium-ion battery
MFCC	metallized film current collector
NMC	lithium nickel manganese cobalt oxide
ORNL	Oak Ridge National Laboratory
PET	polyethylene terephthalate
SOC	state of charge
TCF	Technology Commercialization Fund
XCT	x-ray computed tomography

EXECUTIVE SUMMARY

The US Department of Energy's Oak Ridge National Laboratory and Soteria Battery Innovation Group collaborated to develop a metallized polymer film as a current collector for lithium-ion batteries and design slit patterns for electrodes to improve battery safety. The metallized polymer film serves as a fuse that will break under high temperature resulting from a short circuit. Consequently, the short circuit will be broken and the heat generated from the short circuit will be alleviated to avoid thermal runaway. The electrodes with slit patterns are expected to be broken into small segments upon mechanical impact, which can isolate the damaged electrodes from the rest. Thus, the heat generation associated with the mechanical impact will be reduced, along with the likelihood of thermal runaway.

This effort aimed to improve lithium-ion battery safety by replacing traditional metal foils with metallized polymer films as current collector and introducing slit patterns to battery electrodes. The metallized polymer films were polyethylene terephthalate with a thin metal (aluminum for cathodes and copper for anodes) coating on both sides. Slit patterns with various geometries and dimensions were designed via simulation. Temperature distribution on cells with electrodes with and without slit patterns was also simulated via nemerical modeling. Electrodes on traditional metal foils and metallized polymer films were coated via a pilot-scale slot-die coater at the US Department of Energy Battery Manufacturing Facility at Oak Ridge National Laboratory. The electrodes were calendered to 35% porosity and punched out with and without slit patterns. Pouch cells were assembed with the electrodes inside a dry room for electrochemical and safety testing. Electrodes coated on metallized polymer films exhibited comparable electrochemical performance to their counterparts coated on traditional metal foils. They also showed improved safety in nail penetration and indentation tests.

As a result of this work, one research license has been established from US Patents 10,374,234 B2 and 9,847, 531 B2 through a license agreement number PLA-1967. Three papers will be developed from the project, including one under review and two under preparation.

1. OBJECTIVE

The overall goal of this project is to demonstrate significant improvement in lithium-ion battery (LIB) safety by isolating problem areas caused by electrical shorting and/or physical damage through the US Department of Energy's (DOE's) Oak Ridge National Laboratory's (ORNL's) innovative current collectors and Soteria Battery Innovation Group's metallized polymer films while maintaining comparable cycle life to batteries with conventional current collectors (pouch and cylindrical cells). This project addresses a barrier for commercialization of the novel current collector—the lack of a demonstration of the technology in a large number of commercial cells.

Soteria Battery Innovation Group (Participant) is dedicated to enabling portable electric power without the risk of fires, no matter the circumstances. Soteria has developed a metallized thin film as a current collector for LIBs, where the thin metal coating is thick enough for normal battery operations but melts with very high currents associated with defects and dendrites. As a result, it eliminates battery safety hazard events and enables up to 20% weight reduction of LIBs.

ORNL (Contractor) has developed a technology to mitigate thermal events of LIBs via a safe current collector design. A patent (US Patent 9,847,531) entitled "Current Collectors for Improved Safety" was issued on December 19, 2017. Mechanical abuse of LIBs can lead to complete failure. The developed approach for mitigating the severity of internal electrical shorts in LIBs uses electrodes designed to break upon impact into electrically isolated pieces before the separator is punctured. The electric current passing through the internal short(s) is reduced, preventing the onset of exothermic reactions and thermal runaway. The approach is to create breakable electrodes by cutting partial slits in the electrode and current collectors using traditional metal foils. The whole approach uses the same manufacturing equipment and processes as those for standard electrodes. Thus, the technology can be easily deployed at scale and will not increase manufacturing costs. This technology also allows undamaged portions of the batteries to remain functional once damaged sections have been electrically isolated.

This effort focuses on further developing the slit design, fabricating electrodes on traditional metal foils and Soteria's metallized polymer films, and demonstrating the benefits on safety, cost reduction, and energy improvement in large cells.

2. INTRODUCTION

Progress in electrode engineering and continuous development of new chemistries with high energy density and have enabled dramatical energy density improvement in the past three decades. The ever-growing energy density in LIBs requires innovative designs in batteries to meet safety requirements. Currently, safety of LIBs relies on the separator, a circuit interrupt device, safety vents, and controlling operating conditions. Furthermore, robust packaging is required to protect LIBs from mechanical impacts, which adds additional weight and volume and reduces energy density.

This project aims to improve battery safety through innovations in current collector and electrode design, which does not introduce additional parts to battery packs. Additionally, it reduces the weight and volume because the metallized polymer films are lighter and thinner than traditional metal foils. The whole electrode fabrication and cell assembly process is the same and is compatible with state-of-the-art instruments. Thus, the innovative approaches will not increase manufacturing costs.

3. BENEFITS TO THE FUNDING DOE OFFICE'S MISSION

The work performed under this cooperative research and development agreement (CRADA) directly supports DOE's mission in the Technology Commercialization Fund (TCF) to ensure federal research and development investment in technology with commercial potential in a viable market. The CRADA resulted in a research license of two ORNL patents (US 10,374,234 B2 and US 9,847,531 B2) by Soteria (Agreement Number PLA-1967) in 2020. This is well aligned with TCF's goal to provide an opportunity to support collaboration between DOE facilities and private industry. This CRADA between ORNL and Soteria focuses on further developing slitted electrodes and metallized polymer current collectors and demonstrates the improved battery safety.

4. TECHNICAL DISCUSSION OF WORK PERFORMED BY ALL PARTIES

4.1 DESIGN OF SLIT PATTERNS

The controlled tearing and fragmentation of battery electrodes under deformation has recently been proposed by the authors [1] as a safety mechanism for avoiding an electrical short in batteries. The concept has been illustrated by computational modeling and experiments. The authors used a perforation pattern to enable experimental validation of the computational model. In this study, additional patterns of different topologies and scales were examined to investigate consistency of the approach and trends. The study is based on computational models, and experiments were conducted for validation of the computational models and further concept development.

The original perforation design [1] was based on a rectangular pattern in which, when the battery electrode is subjected to in-plane uni- or biaxial tension, it leads to rotation of square foil patches that drive tearing crack propagation in the foil and fragment it. Indentation of the foil in the direction orthogonal to its plane induces biaxial stretching in the foil. The perforation pattern is such that cracks open in a symmetric opening mode. In the parlance of fracture mechanics, this is a K-1 crack propagation mode, although a concept of tearing and crack propagation in thin foils is still under development [2-9]. The developed quadrilateral perforation pattern has cracks growing toward free surfaces, which are natural attractors for crack propagation. The cracks in this study are associated with tearing of the foils which, as noted, still have to be defined using new mechanics theories.

In the current work, in addition to variations of the original quadratic perforation pattern, a new triangular perforation pattern was investigated that has similar fragmentation promoting kinematics under foil in-plane tension. The models are based on the finite element (FE) method [10]. Simulations were conducted using the FE modeling software LS-DYNA [11].

4.1.1 FE Models

The perforation patterns and their respective FE models developed in this study are shown in Figure 1–Figure 12. Figure 13–Figure 16 show the details of the FE model illustrating control of the FE discretization and element topology. The unit cell parameters, c, L, and $a = c/L$, are denoted in Figure 17 and Figure 18 for the two main topological patterns. Configuration of the perforation for each of the perforation topologies was determined by the values of L and c parameters. The resulting perforation topology models were scaled to sizes of unit cells (L) of 6.4, 8, and 10 mm, which for 10 repeated unit cells gave model spans of 64, 80, and 100 mm, respectively. The model parameters resulted in 18 distinct perforation configurations and FE models. The perforated foils were modeled by thick shell elements with five integration points. The thickness of the foil was 10 μm. The foil material was copper and was modeled as elastoplastic material. The indentation was modeled as a steel sphere with a radius of 40 mm that is driven into the center of the foil sheet by constant velocity. The friction coefficient between the indentation and sphere was 0.1. Stress concentrations at the tips of the perforation patterns were observed and persisted with increasing indentation. The indentation leads to rotation of foil patches and continuously increasing stress concentrations, which are expected to result in tearing and fragmentation.

Tearing fracture models based on element deletion were also tried, and although they showed some general resemblance to the fracture process, they did not have sufficient resolution, and they lack foil tearing fracture models and parameters. Therefore, the investigation was restricted to confirming anticipated deformation kinematics prior to tearing and fragmentation, as well as stress concentrations that would drive them.

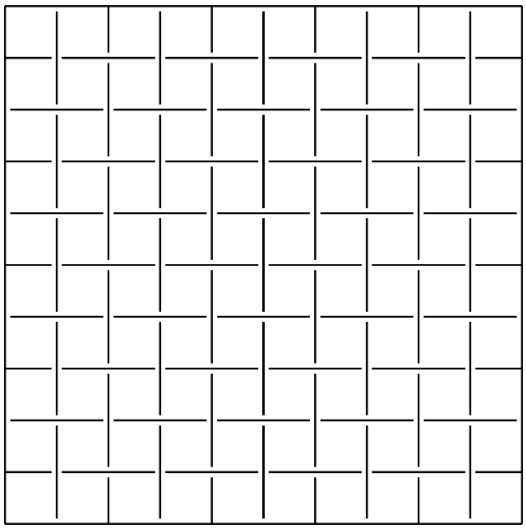

Figure 1. Quad pattern, *a* = 0.1.

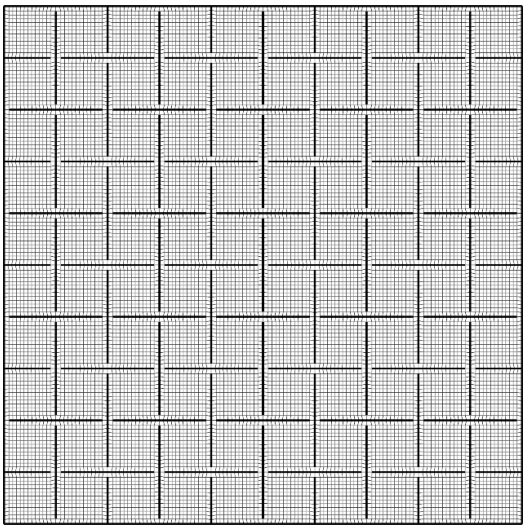

Figure 2. Quad pattern FE model, *a* = 0.1.

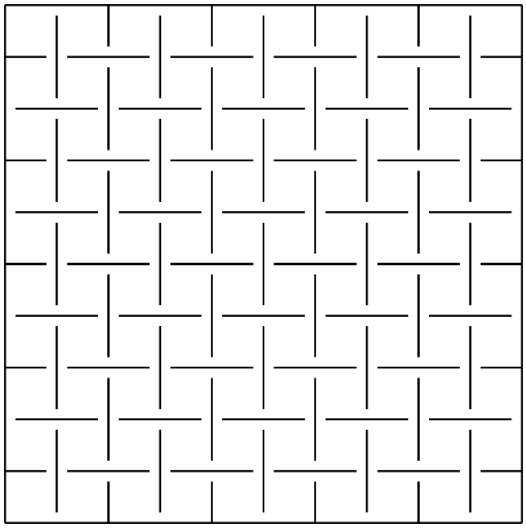

Figure 3. Quad pattern, *a* = 0.2.

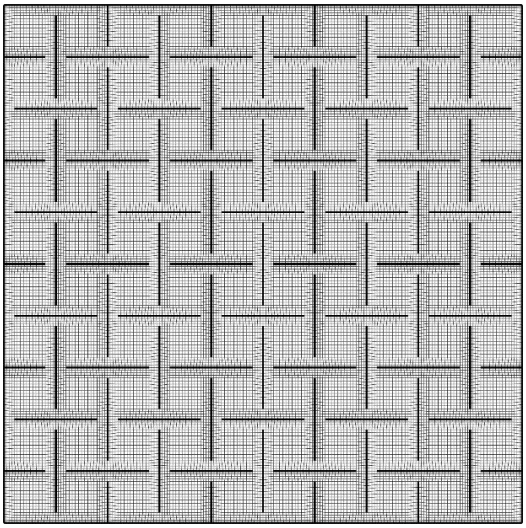

Figure 4. Quad pattern FE model, *a* = 0.2.

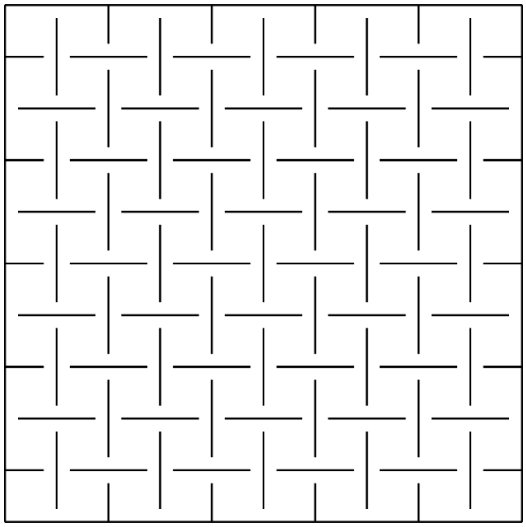

Figure 5. Quad pattern, *a* = 0.25.

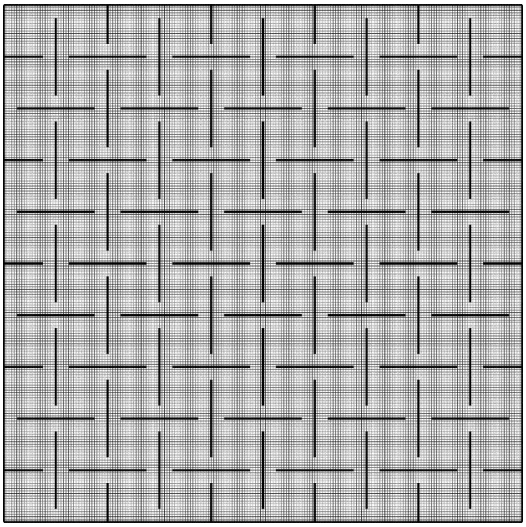

Figure 6. Quad pattern FE model, *a* = 0.25.

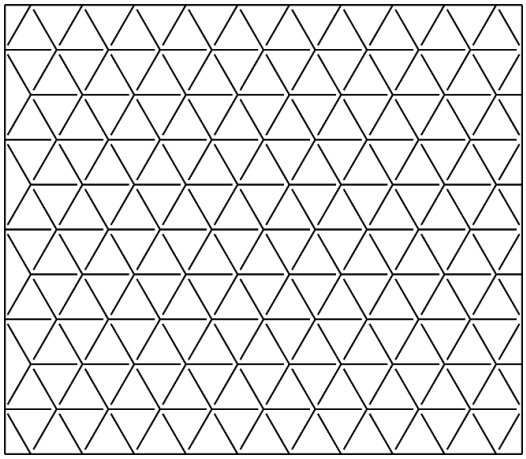

Figure 7. Triangle pattern, *a* = 0.1.

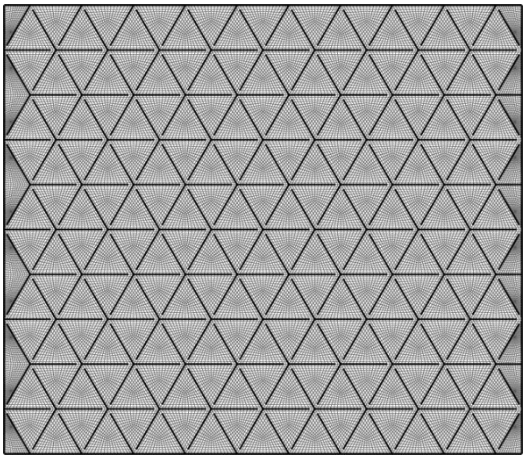

Figure 8. Triangle pattern FE model, *a* = 0.1.

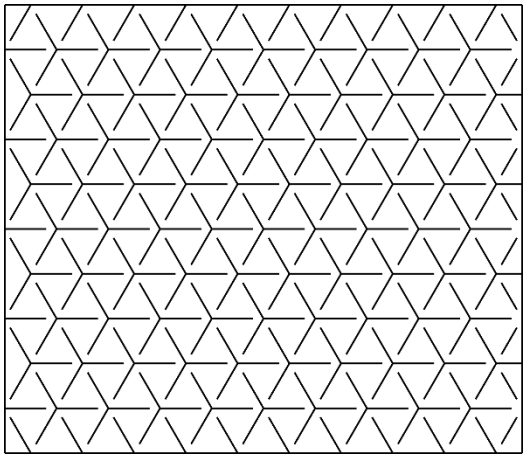

Figure 9. Triangle pattern, *a* = 0.2.

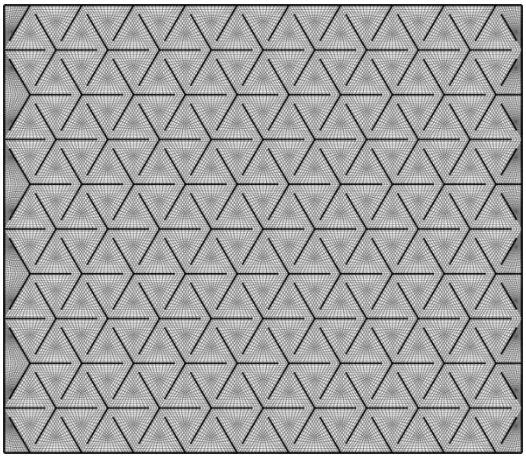

Figure 10. Triangle pattern FE model, *a* = 0.2.

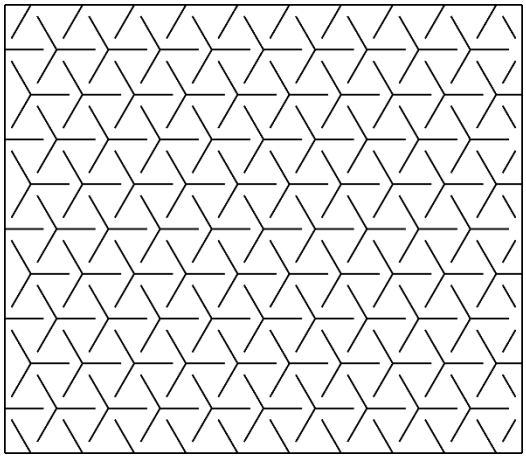

Figure 11. Triangle pattern, *a* = 0.25.

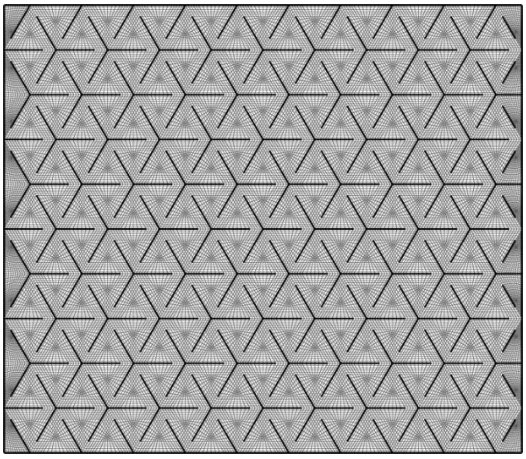

Figure 12. Triangle pattern FE model, *a* = 0.25.

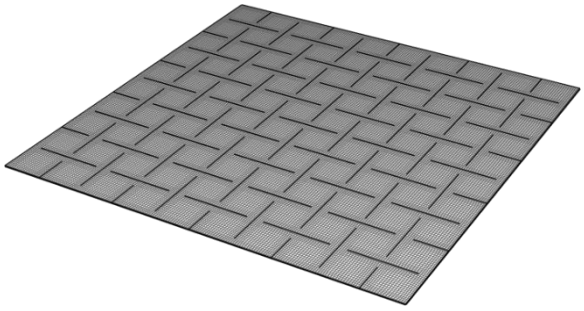

Figure 13. Quad pattern FE model.

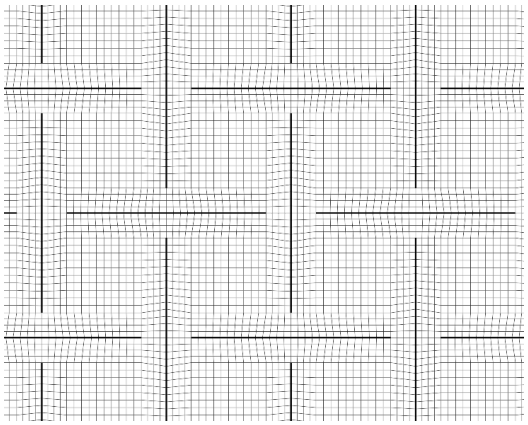

Figure 14. Quad pattern FE model zoom.

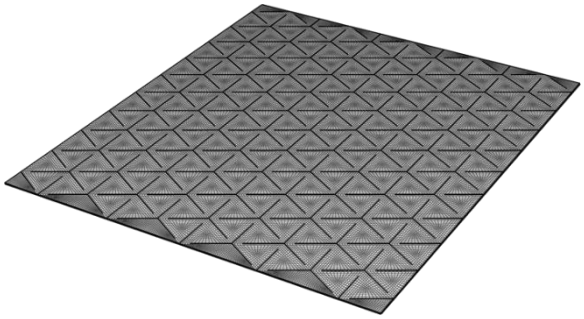

Figure 15. Triangle pattern FE model.

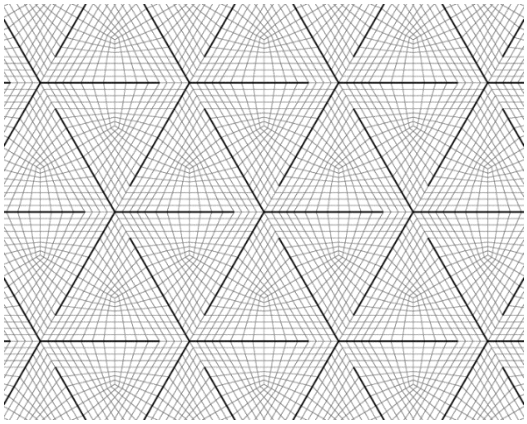

Figure 16. Triangle pattern FE model zoom.

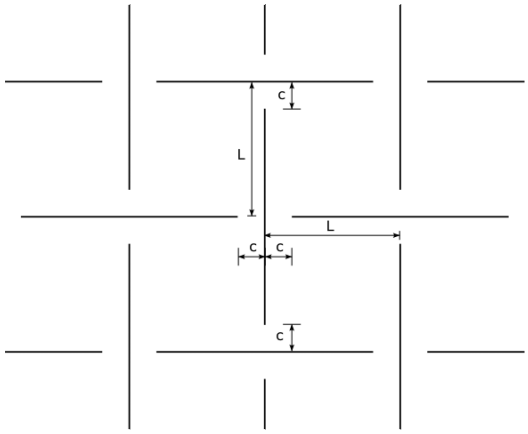

Figure 17. Quad pattern parameters, *a = c/L*.

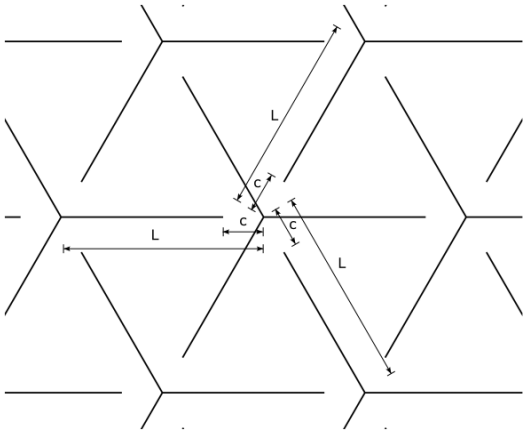

Figure 18. Triangle pattern parameters, *a = c/L*.

4.1.2 Model Results

In this section, results of the computational simulations are provided for various perforation parameters and topologies. In addition to the quadratic perforation pattern presented in the original work [1], a new triangular perforation pattern was developed and tested for deformation kinematics that is compatible with fragmentation under indentation.

The deformation of a foil perforated in a quadratic pattern and indented by a rigid sphere with a radius of 40 mm at two stages of indentation (10 and 20 mm) is shown in Figure 19.

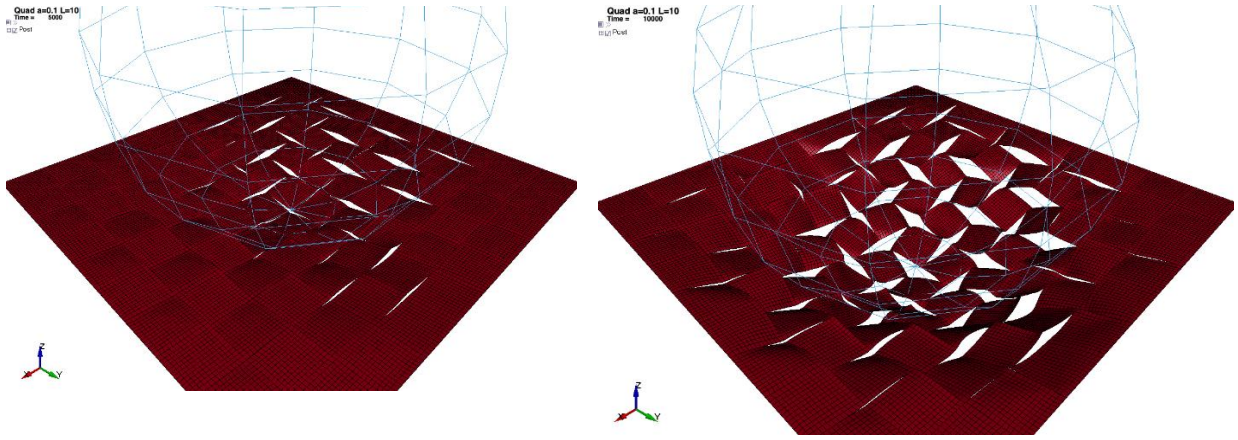

(a) (b)

Figure 19. Deformation of a perforated foil at two stages of indentation by a sphere: (a) indentation of 10 mm and (b) indentation of 20 mm.

The deformation of the indented foil from under the foil was observed, and distributions of effective stresses and strains at an indentation of 10 mm and 20 mm were compared. For the foil dimensions considered in this study, the stress concentrations at 20 mm indentation will likely be sufficient to drive crack propagation.

4.1.3 Indentation of Foils Perforated in Quadratic Pattern

For a crack to initiate and propagate, the relative size of the unbroken ligament with respect to the crack opening is the most important parameter. Therefore, in addition to presenting the results by the topology of the perforation pattern, the models were organized by the relative size of the ligament and then by the size of the unit patch.

The first model had quadratic pattern perforation, relative ligament size $a = c/L = 0.1$, and $L = 10$ mm. This was the smallest relative ligament length considered. Such small ligaments would likely be impractical given the state of current cutting technology. Figure 20 and Figure 21 show the effective plastic strain and effective stress, respectively. The steep stress increase at the perforation tips will promote tearing and disassociation of the foil. Stresses are concentrated in perforation tips, which will drive tearing and fragmentation.

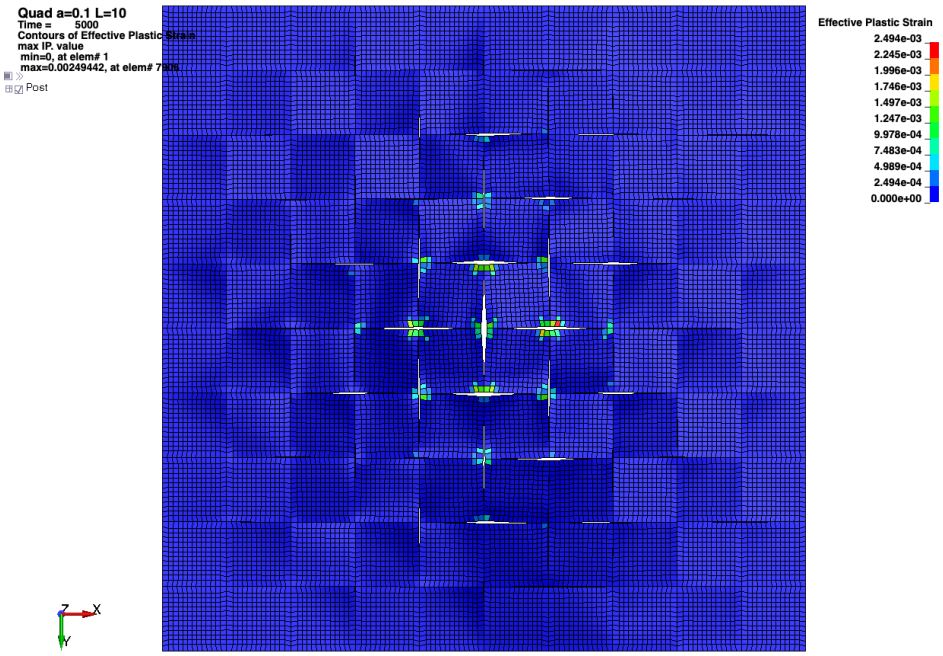

Figure 20. Effective plastic strain in copper foil at indentation of 10 mm, a = 0.1, L = 10 mm.

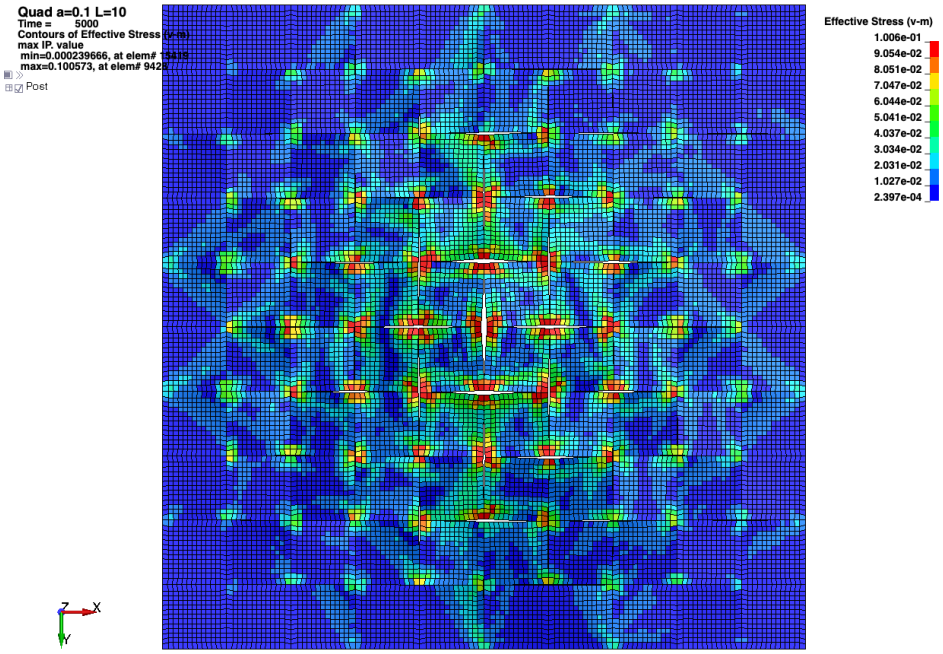

Figure 21. Effective stress in copper foil at indentation of 10 mm, a = 0.1, L = 10 mm.

The next model had quadratic pattern perforation, relative ligament size $a = c/L = 0.1$, and $L = 6.4$ mm. The stresses and plastic strain magnitudes were the largest compared with other perforation patterns. Results for effective plastic strain and effective stress are shown in Figure 22 and Figure 23, respectively.

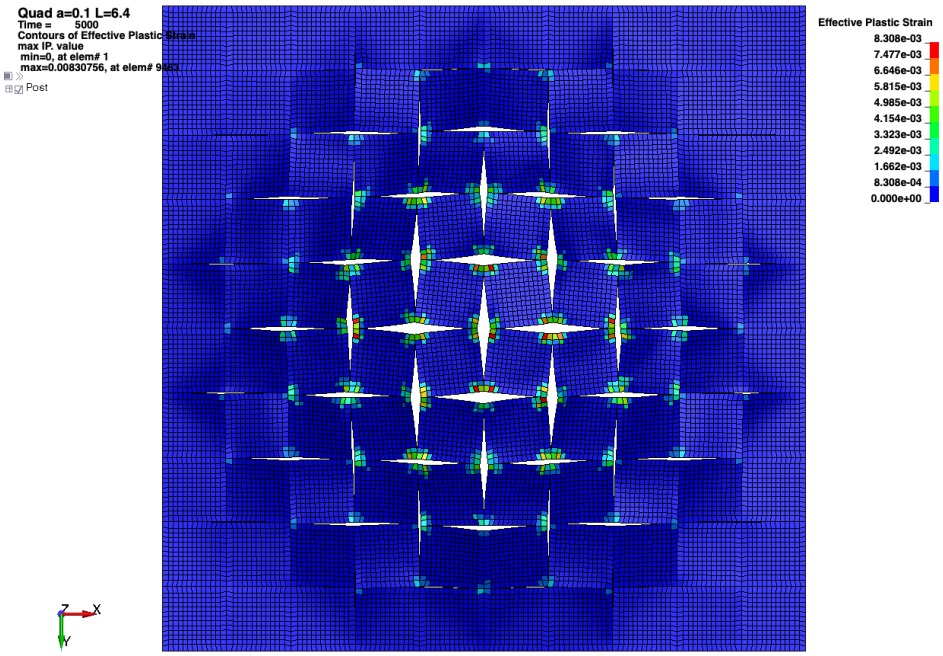

Figure 22. Effective plastic strain in copper foil at indentation of 10 mm, a = 0.1, L = 6.4 mm.

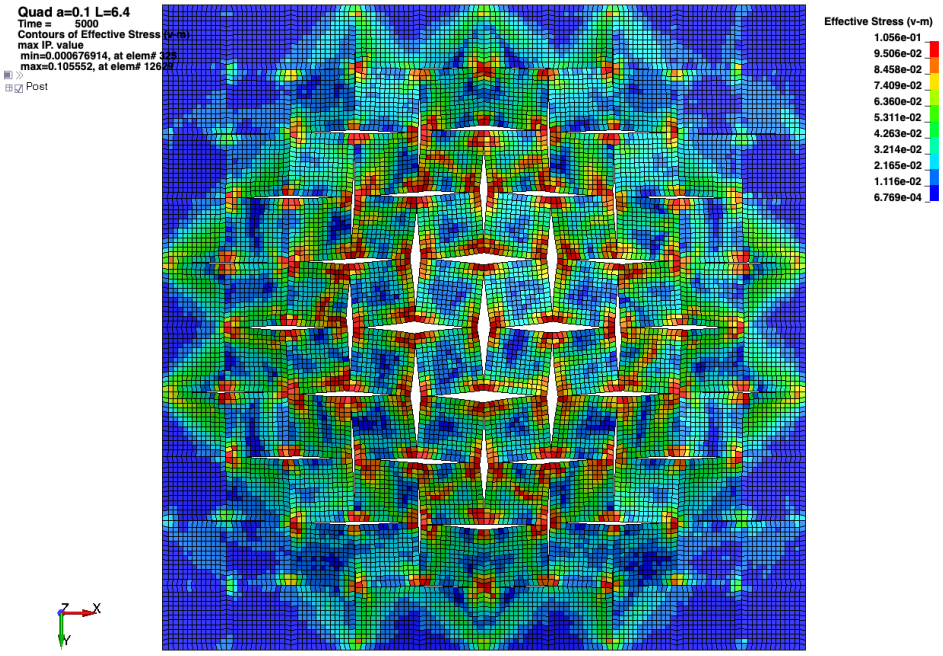

Figure 23. Effective stress in copper foil at indentation of 10 mm, a = 0.1, L = 6.4 mm.

Figure 24 and Figure 25 show simulation results for patterns with perforation parameters of a = 0.1 and L = 8 mm. The maximum stresses and strains occur for the smallest unit cell and decrease with increasing unit cell size.

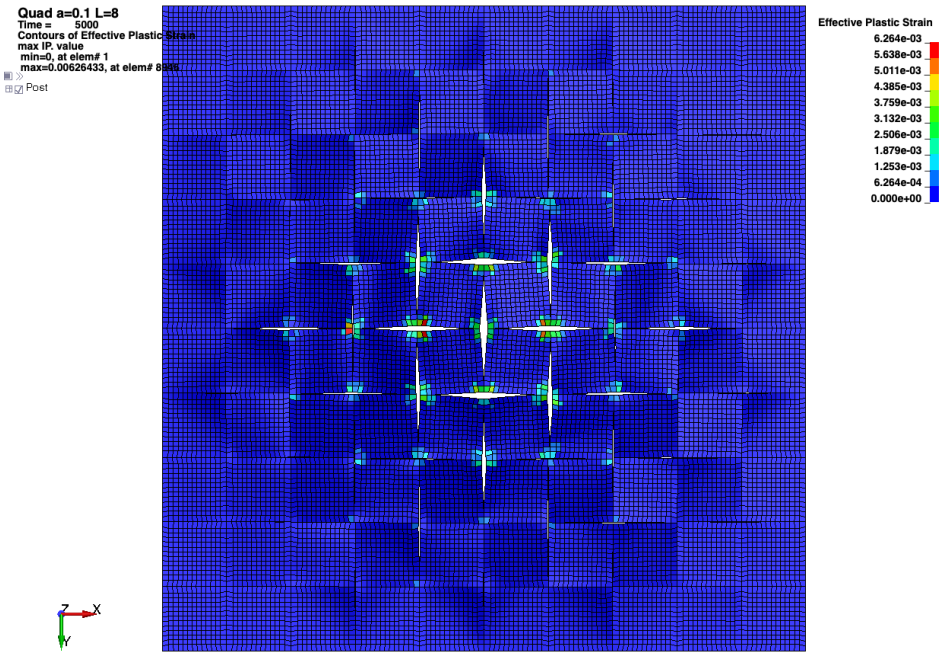

Figure 24. Effective plastic strain in copper foil at indentation of 10 mm, a = 0.1, L = 8 mm.

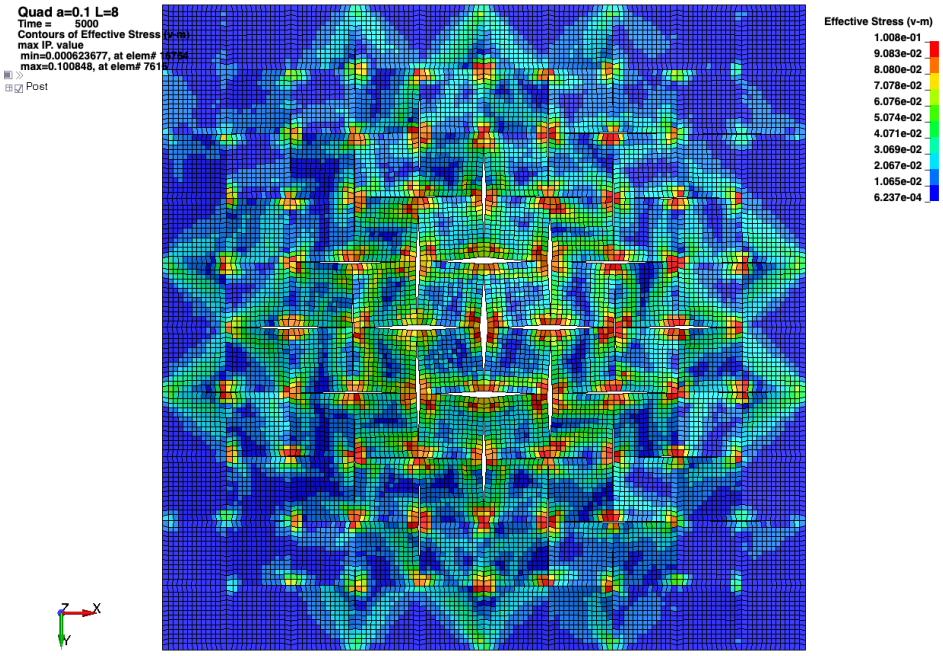

Figure 25. Effective stress in copper foil at indentation of 10 mm, a = 0.1, L = 8 mm.

Figure 26–Figure 31 show the results of the simulations for the relative ligament size of a = 0.2.

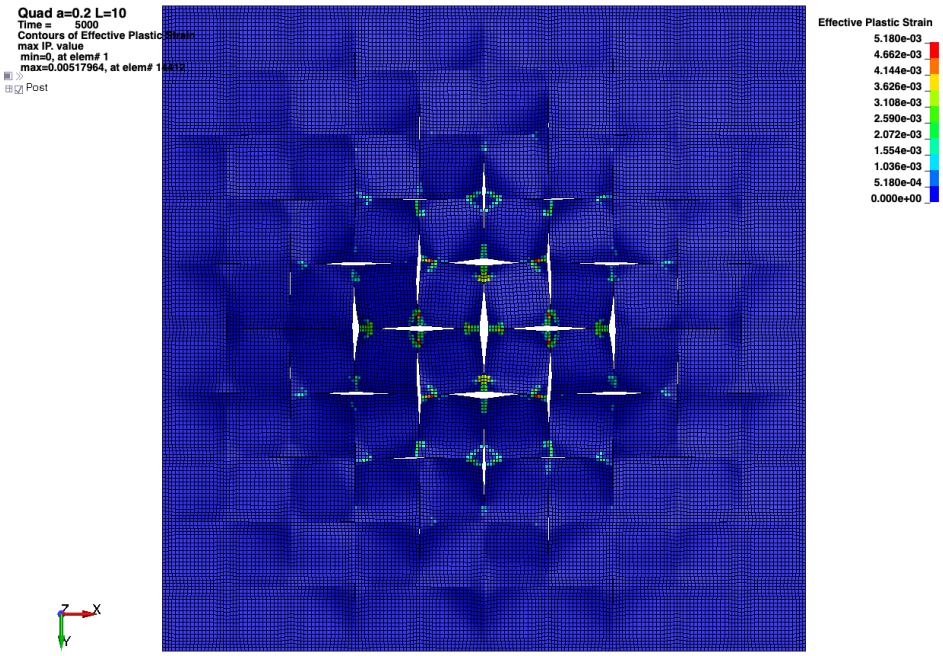

Figure 26. Effective plastic strain in copper foil at indentation of 10 mm, a = 0.2, L = 10 mm.

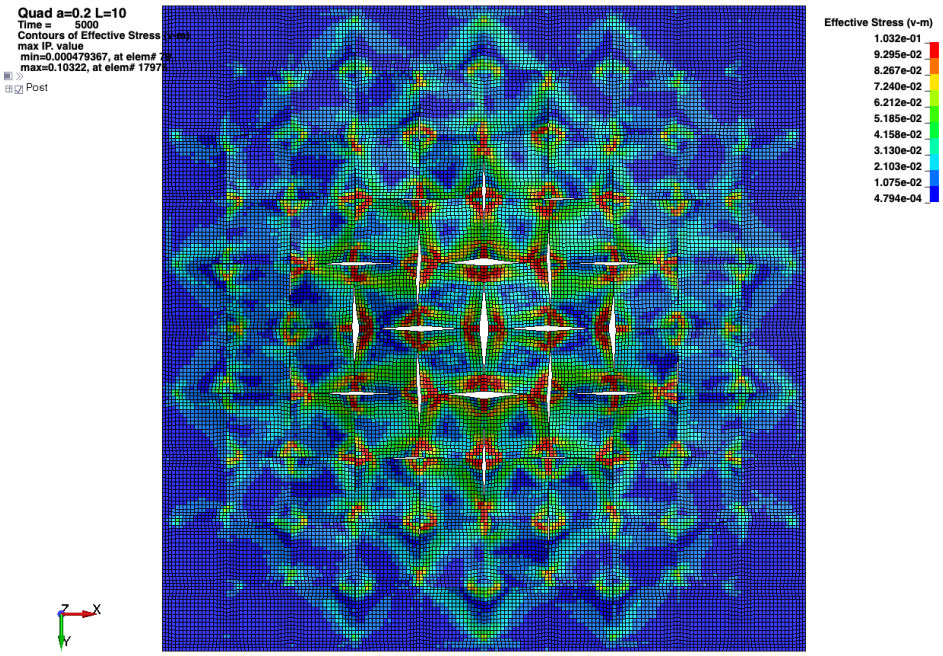

Figure 27. Effective stress in copper foil at indentation of 10 mm, a = 0.2, L = 10 mm.

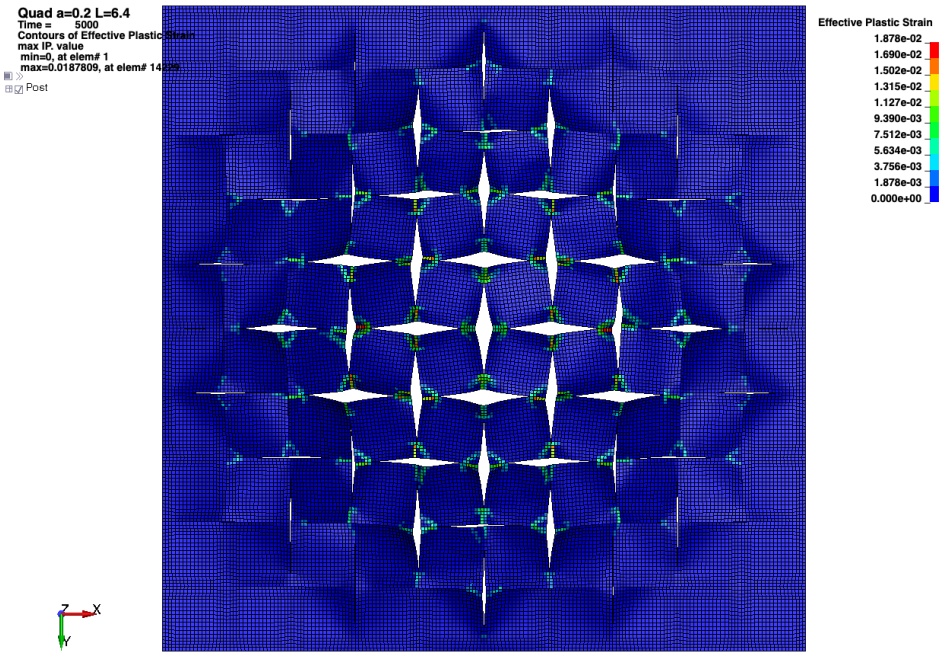

Figure 28. Effective plastic strain in copper foil at indentation of 10 mm, a = 0.2, L = 6.4 mm.

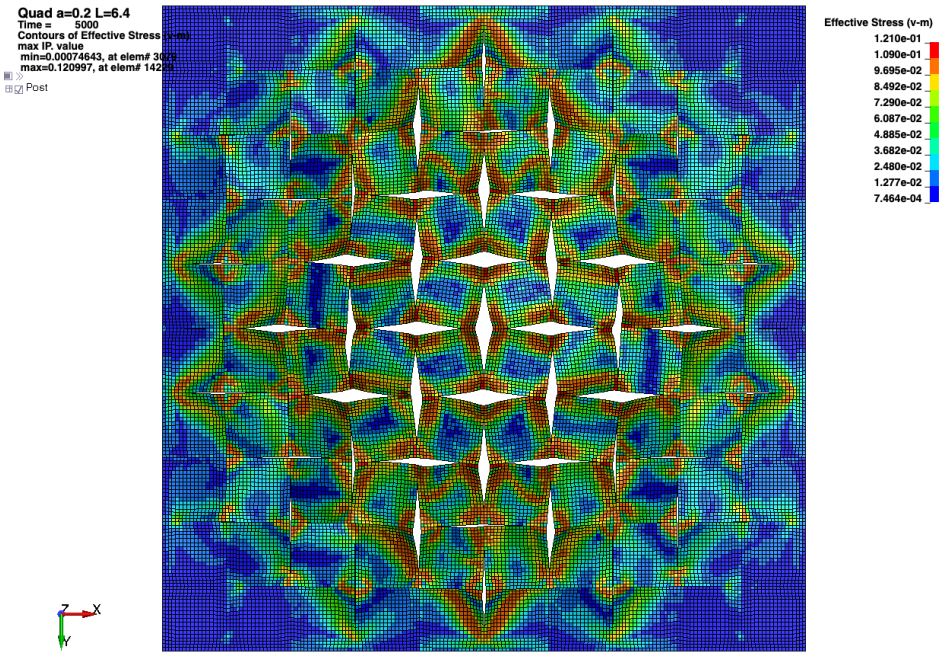

Figure 29. Effective stress in copper foil at indentation of 10 mm, a = 0.2, L = 6.4 mm.

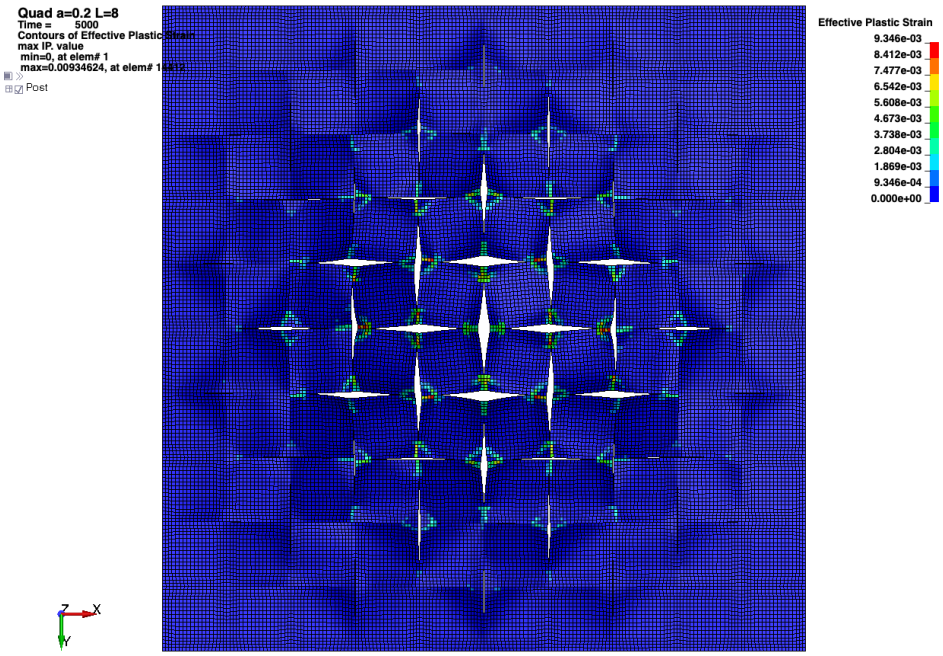

Figure 30. Effective plastic strain in copper foil at indentation of 10 mm, a = 0.2, L = 8 mm.

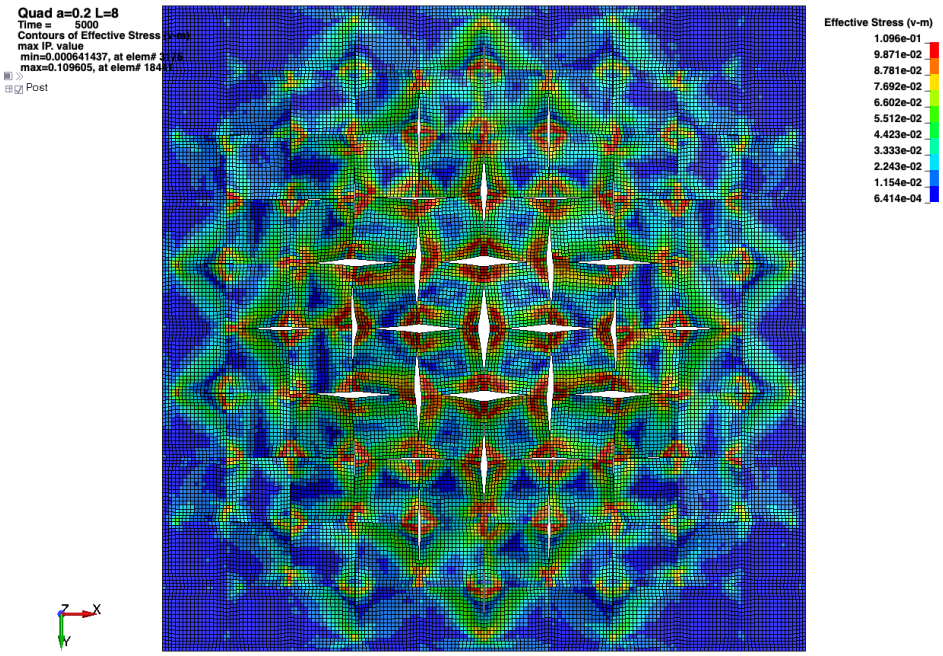

Figure 31. Effective stress in copper foil at indentation of 10 mm, a = 0.2, L = 8 mm.

Figure 32–Figure 37 show simulation results for a = 0.25.

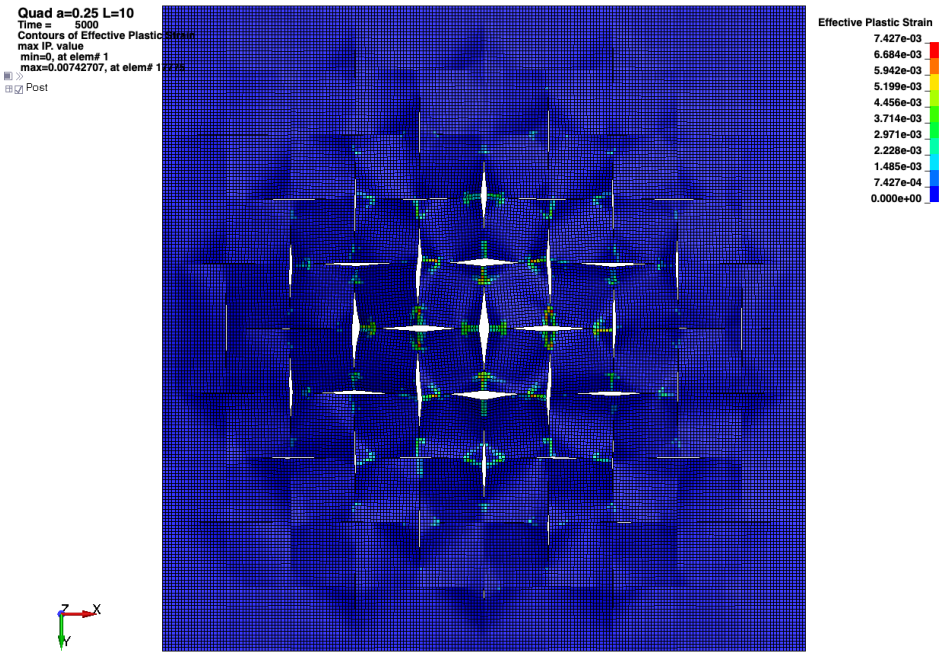

Figure 32. Effective plastic strain in copper foil at indentation of 10 mm, a = 0.25, L = 10 mm.

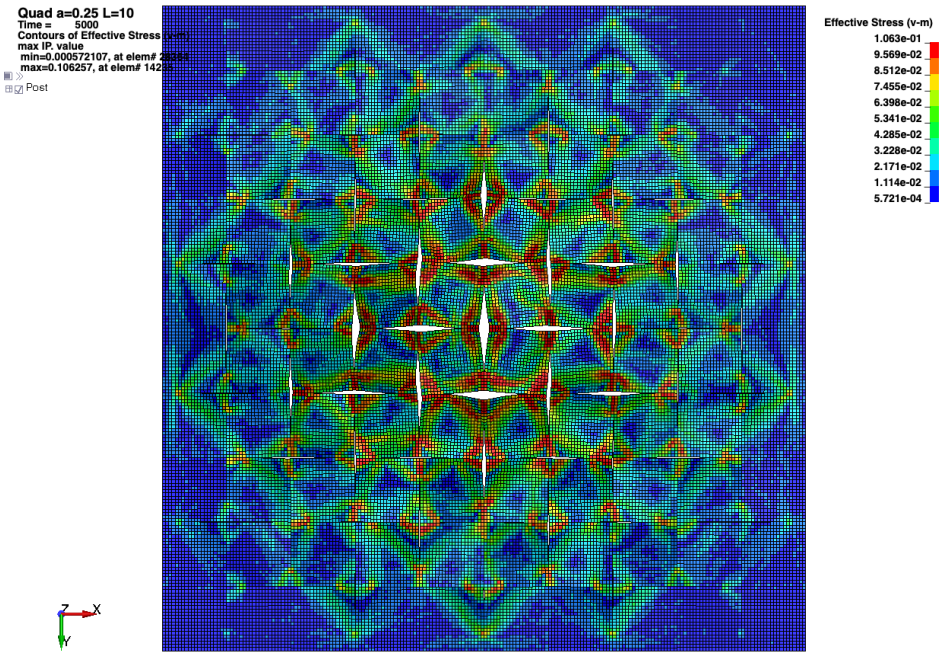

Figure 33. Effective stress in copper foil at indentation of 10 mm, a = 0.25, L = 10 mm.

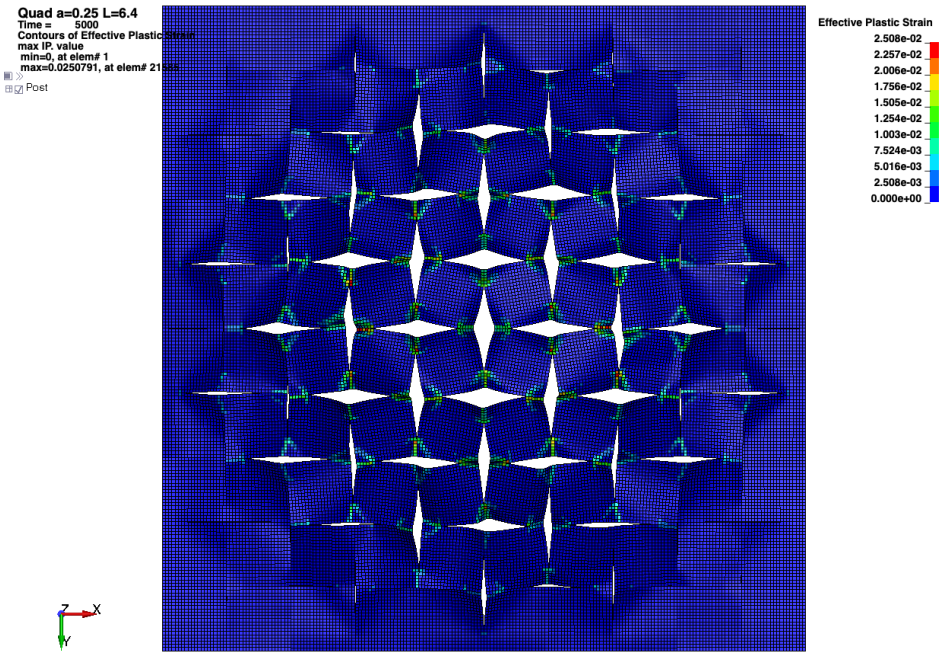

Figure 34. Effective plastic strain in copper foil at indentation of 10 mm, a = 0.25, L = 6.4 mm.

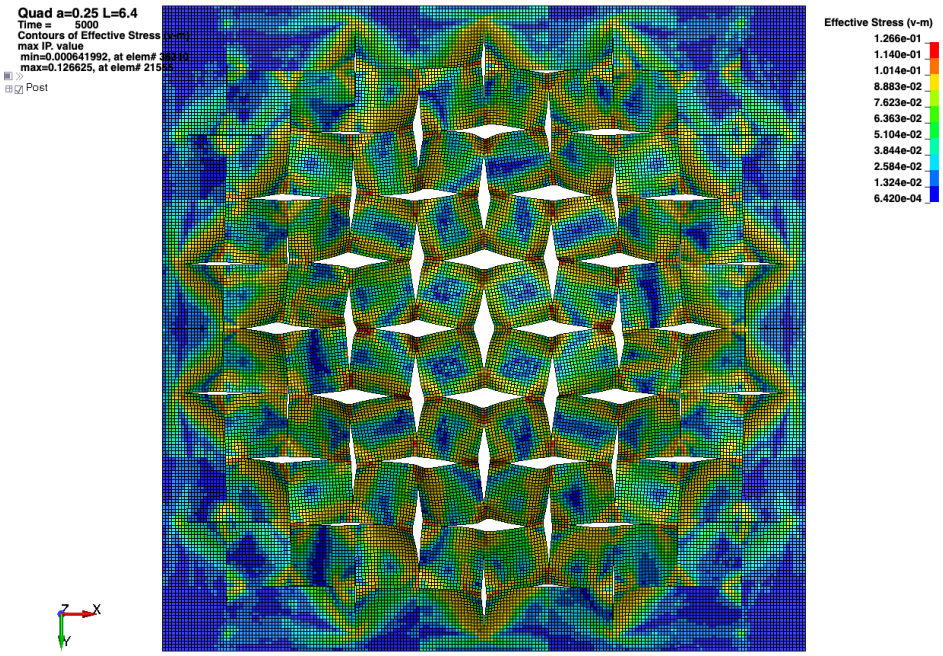

Figure 35. Effective stress in copper foil at indentation of 10 mm, a = 0.25, L = 6.4 mm.

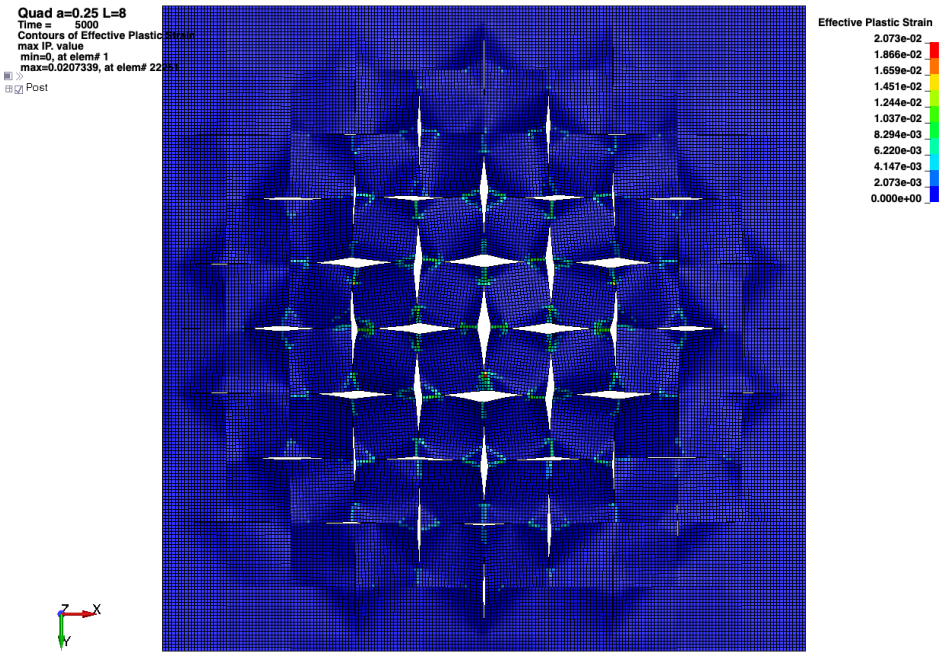

Figure 36. Effective plastic strain in copper foil at indentation of 10 mm, *a* = 0.25, *L* = 8 mm.

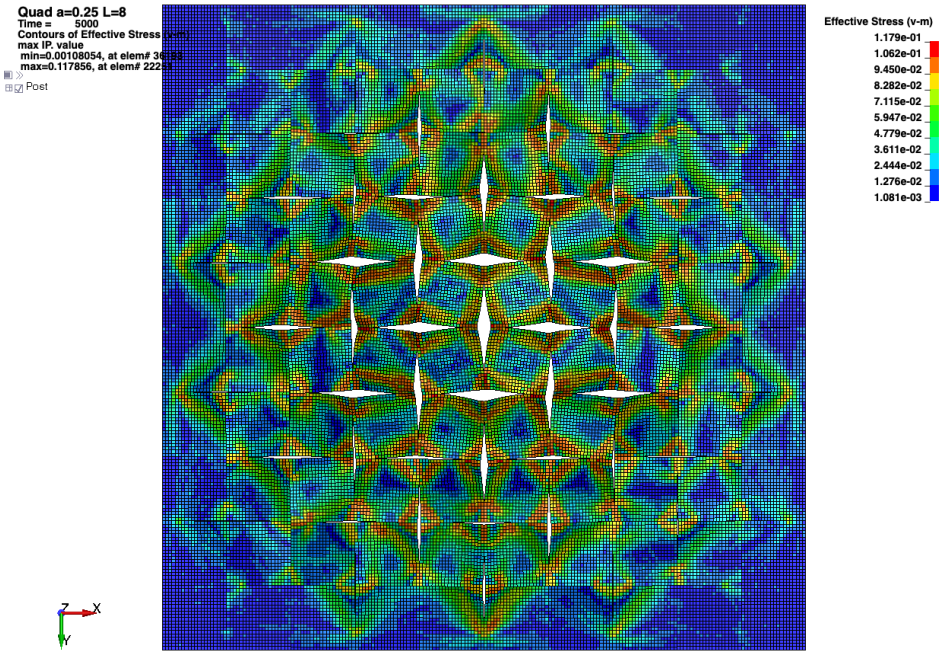

Figure 37. Effective stress in copper foil at indentation of 10 mm, *a* = 0.25, *L* = 8 mm.

All the perforation patterns show similar deformation kinematics and magnitudes of effective strains and stresses that scale with ligament size and unit cell size. The maximum stresses and strains in the ligament regions occur for the smallest unit cell and decrease with increasing unit cell size. The stress concentration increases with deformation, which is expected to reinforce crack growth.

4.1.4 Indentation of Foils Perforated in Triangular Pattern

The deformation, kinematics, effective plastic strain, and effective stress are shown for the new triangular pattern in Figure 38 to Figure 55. This pattern opens up the foil in three principal directions and is more flexible than the quadratic pattern. As with the quadratic patterns, scaling of stresses and strain primarily depends on the relative ligament size and unit cell size. The global kinematics has rotation of foil patches around the ligaments and concentrating stresses in the junctions between the foils. This will drive foil tearing and fragmentation.

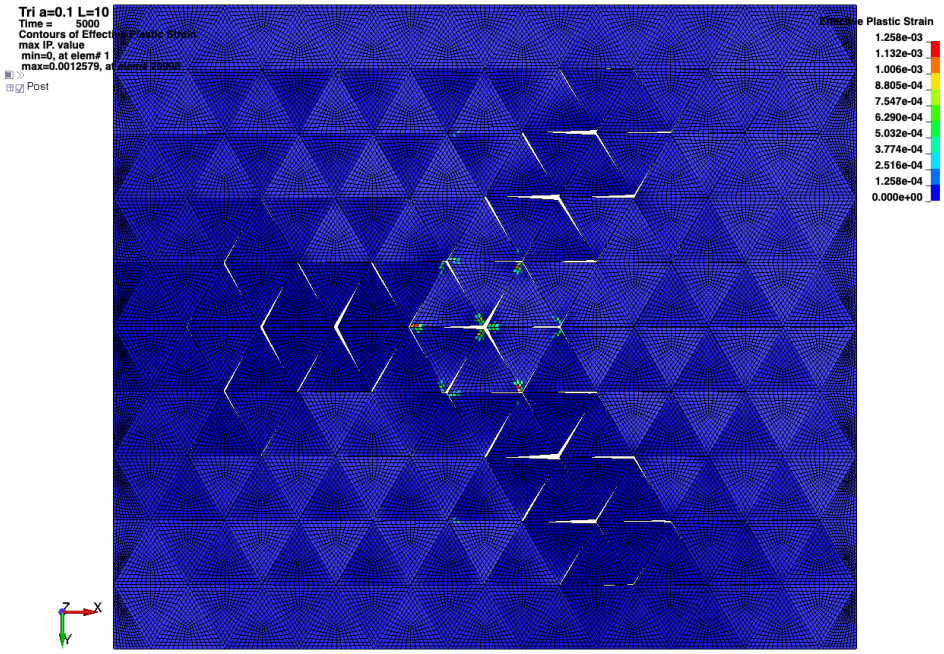

Figure 38. Effective plastic strain in copper foil at indentation of 10 mm, a = 0.1, L = 10 mm.

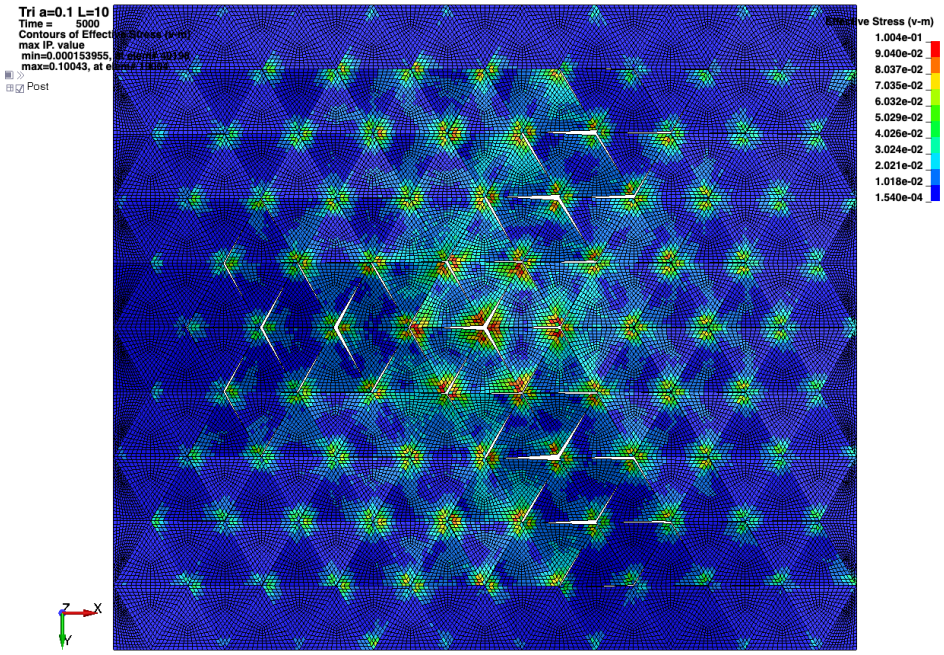

Figure 39. Effective stress in copper foil at indentation of 10 mm, a = 0.1, L = 10 mm.

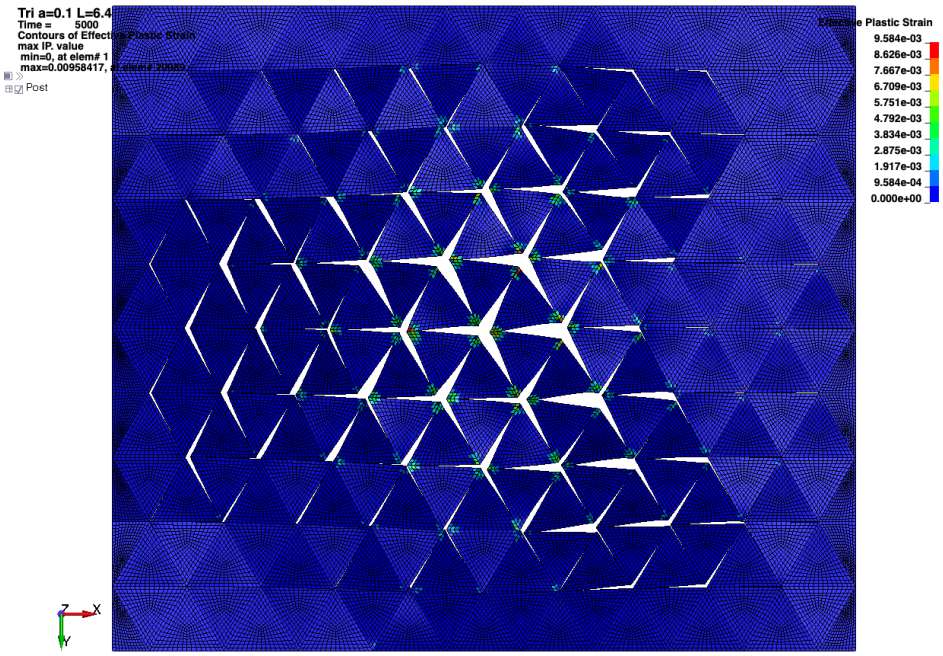

Figure 40. Effective plastic strain in copper foil at indentation of 10 mm, a = 0.1, L = 6.4 mm.

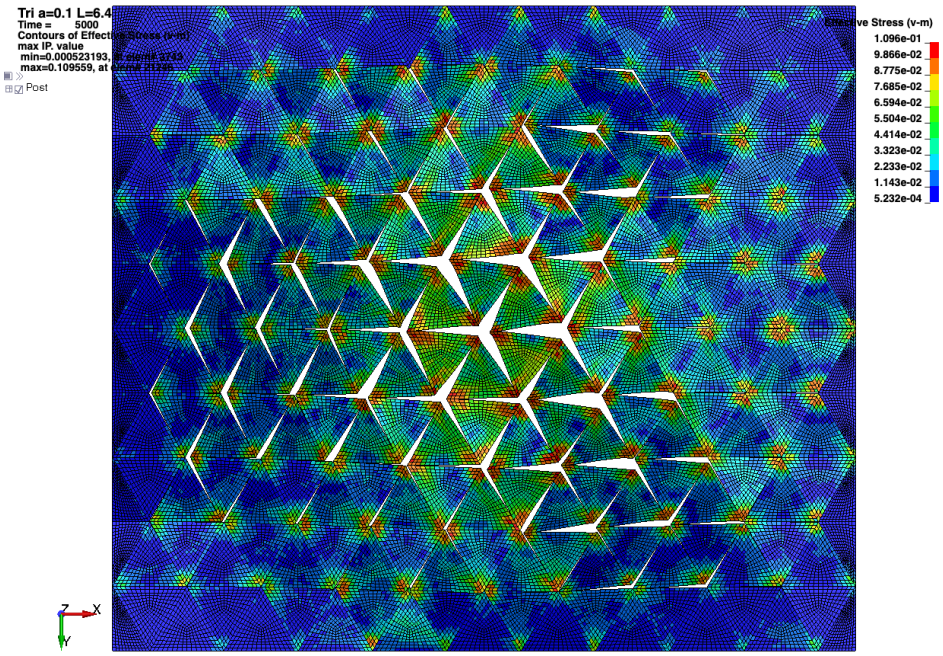

Figure 41. Effective stress in copper foil at indentation of 10 mm, a = 0.1, L = 6.4 mm.

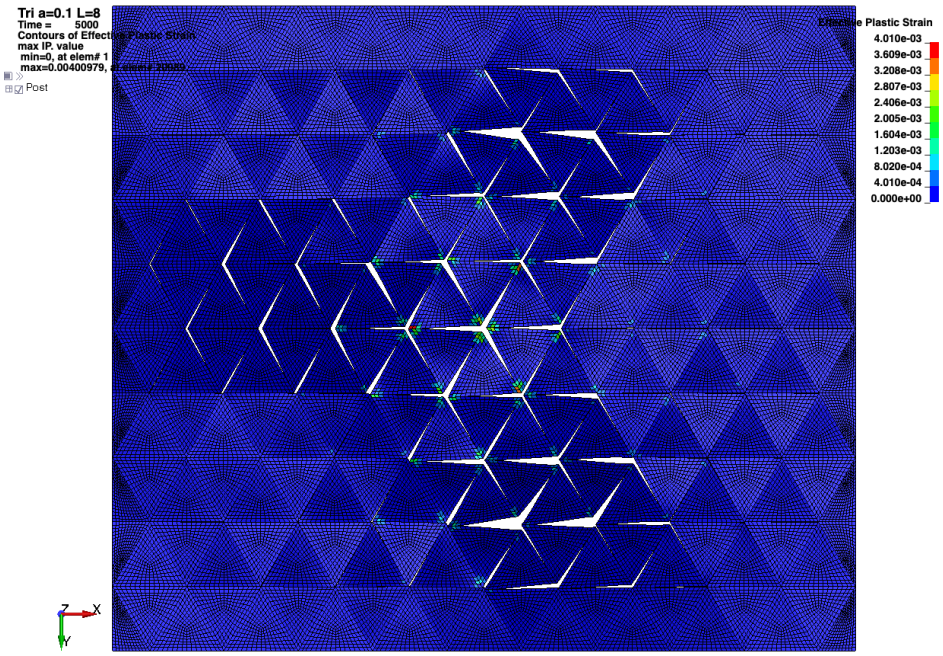

Figure 42. Effective plastic strain in copper foil at indentation of 10 mm, a = 0.1, L = 8 mm.

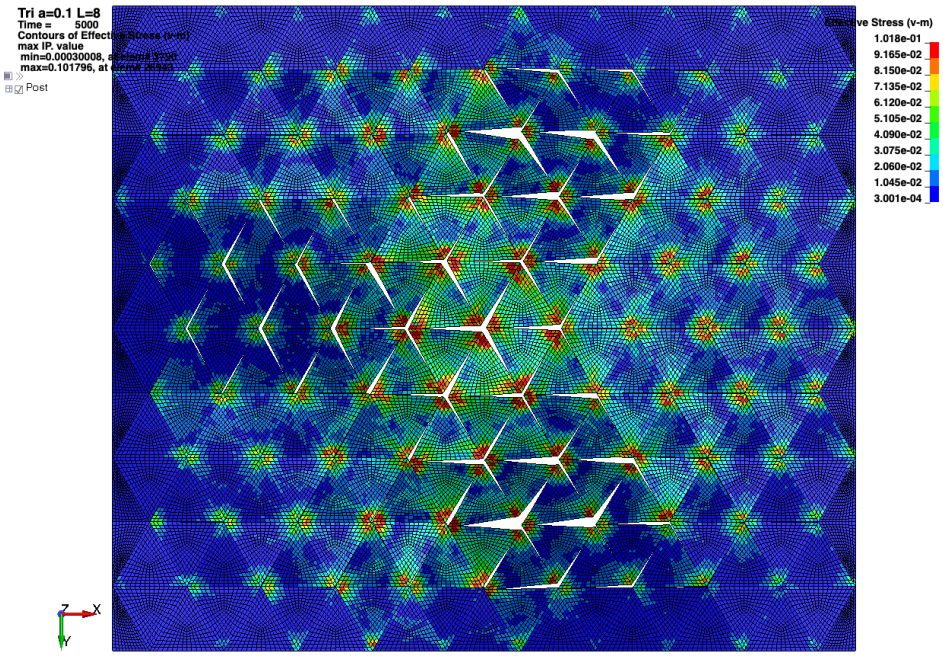

Figure 43. Effective stress in copper foil at indentation of 10 mm, a = 0.1, L = 8 mm.

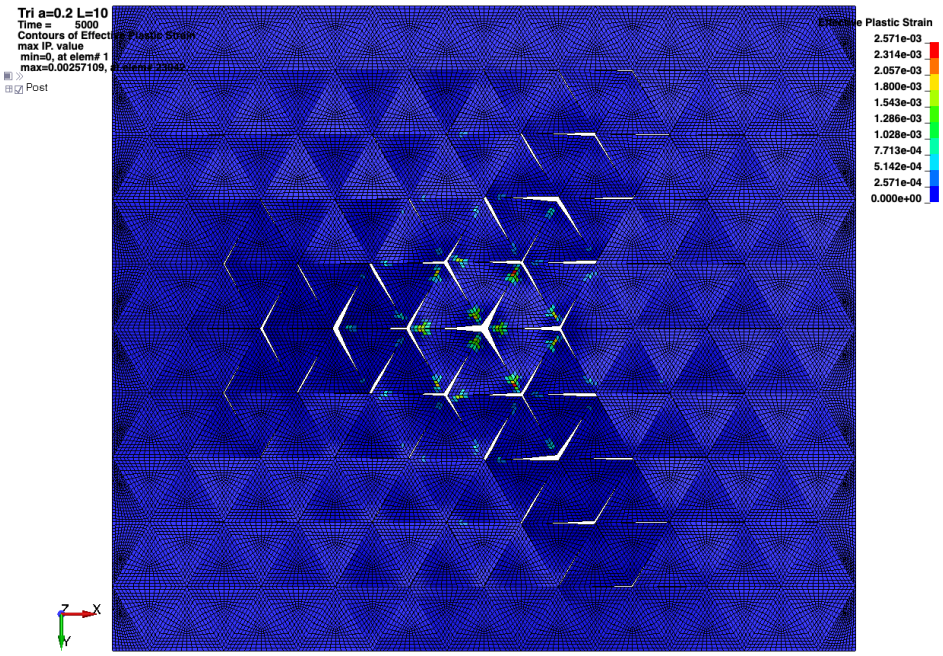

Figure 44. Effective plastic strain in copper foil at indentation of 10 mm, a = 0.2, L = 10 mm.

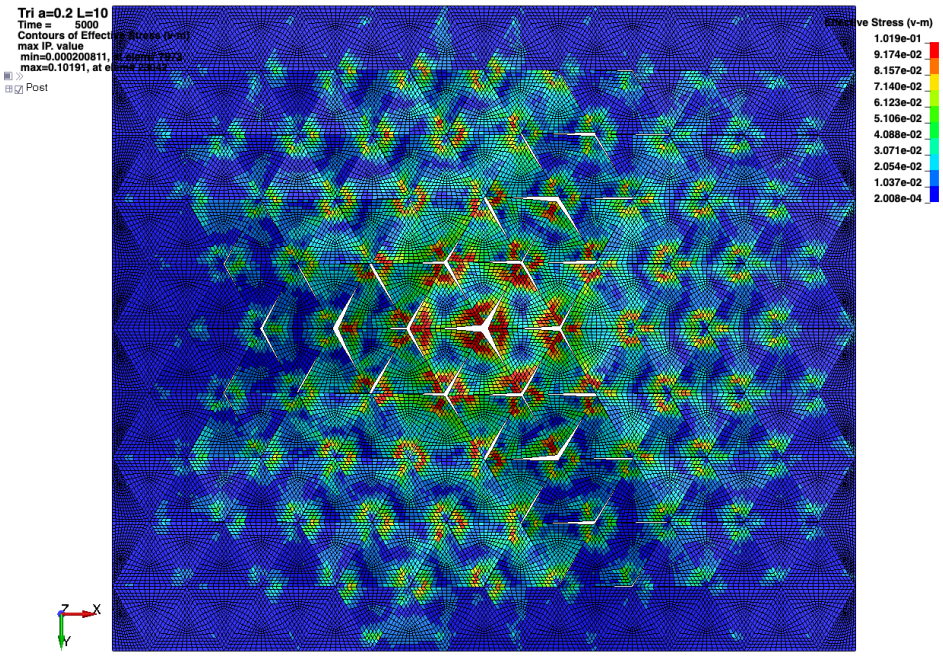

Figure 45. Effective stress in copper foil at indentation of 10 mm, a = 0.2, L = 10 mm.

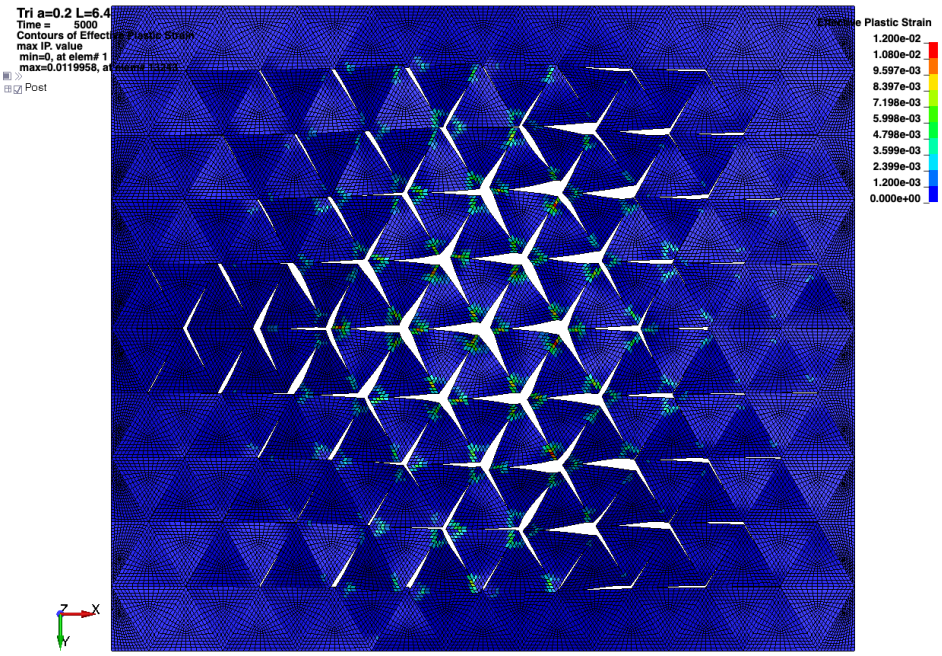

Figure 46. Effective plastic strain in copper foil at indentation of 10 mm, a = 0.2, L = 6.4 mm.

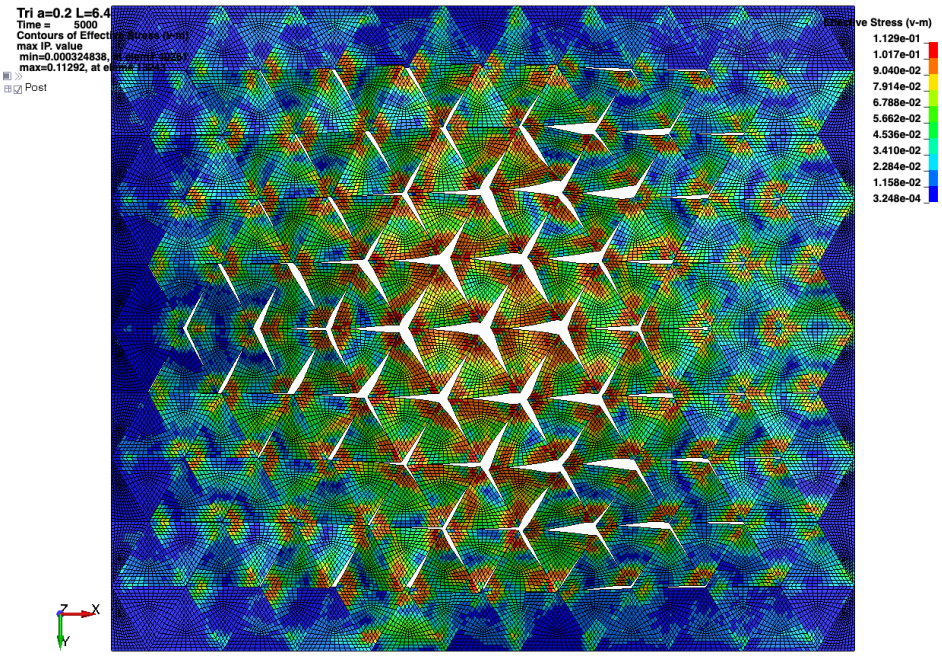

Figure 47. Effective stress in copper foil at indentation of 10 mm, a = 0.2, L = 6.4 mm.

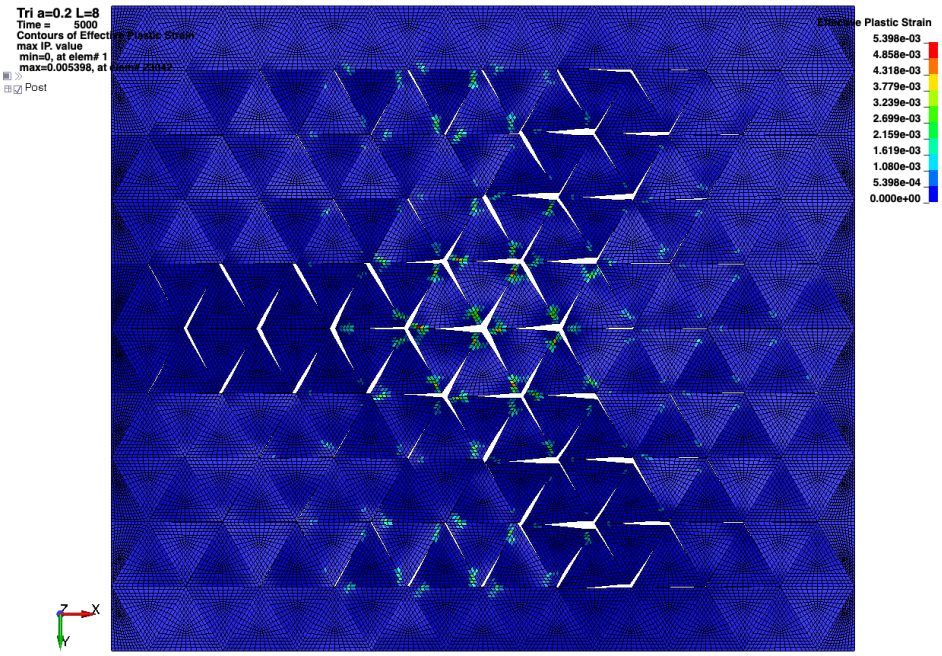

Figure 48. Effective plastic strain in copper foil at indentation of 10 mm, a = 0.2, L = 8 mm.

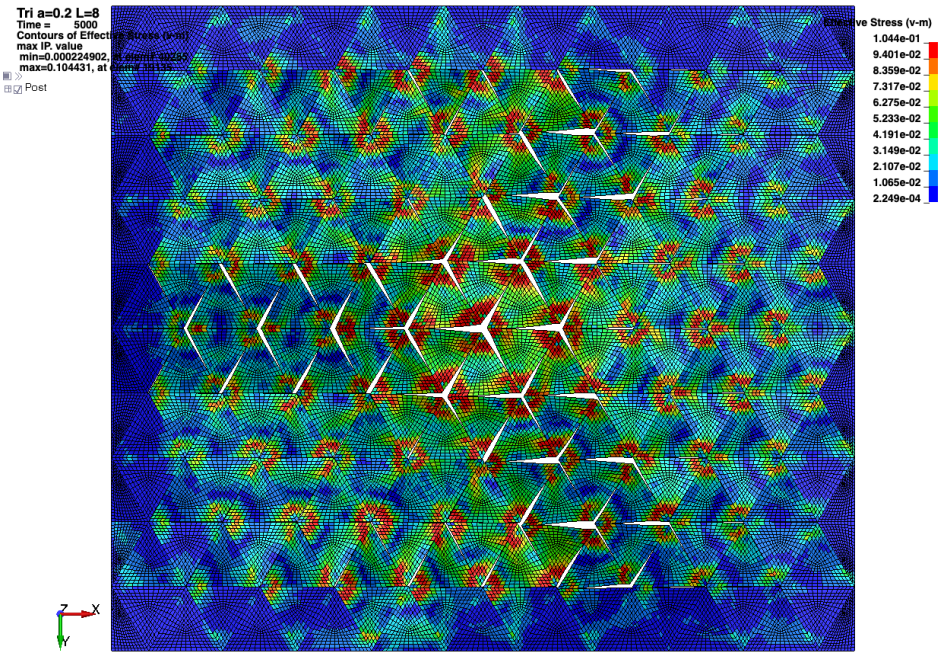

Figure 49. Effective stress in copper foil at indentation of 10 mm, a = 0.2, L = 8 mm.

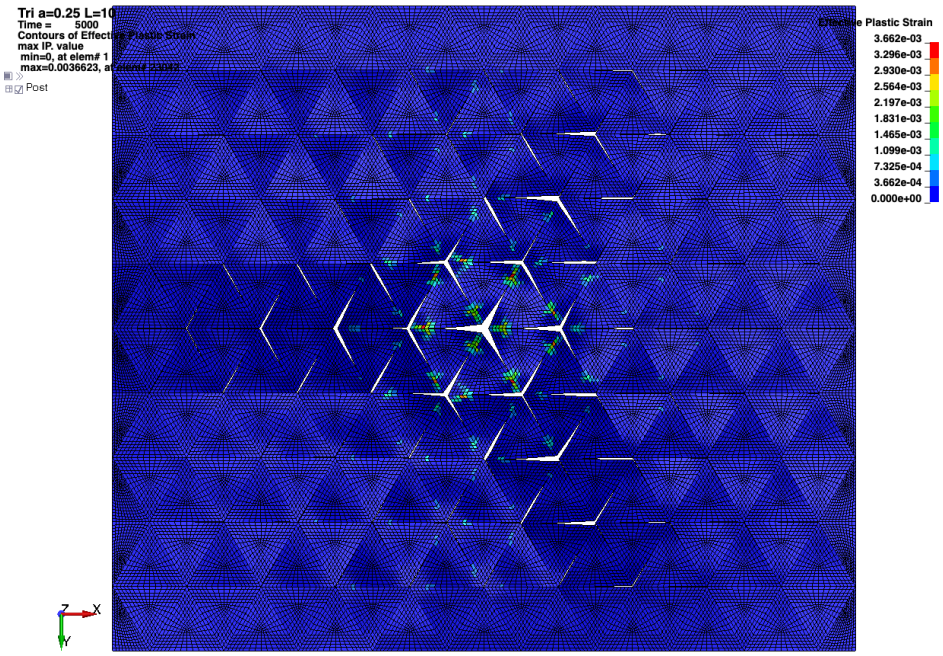

Figure 50. Effective plastic strain in copper foil at indentation of 10 mm, a = 0.25, L = 10 mm.

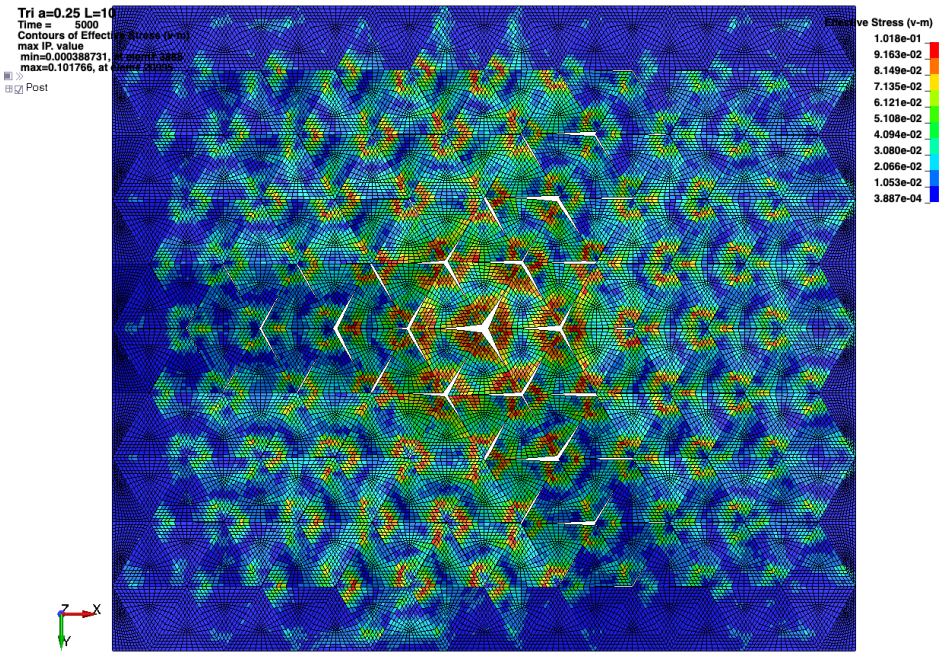

Figure 51. Effective stress in copper foil at indentation of 10 mm, a = 0.25, L = 10 mm.

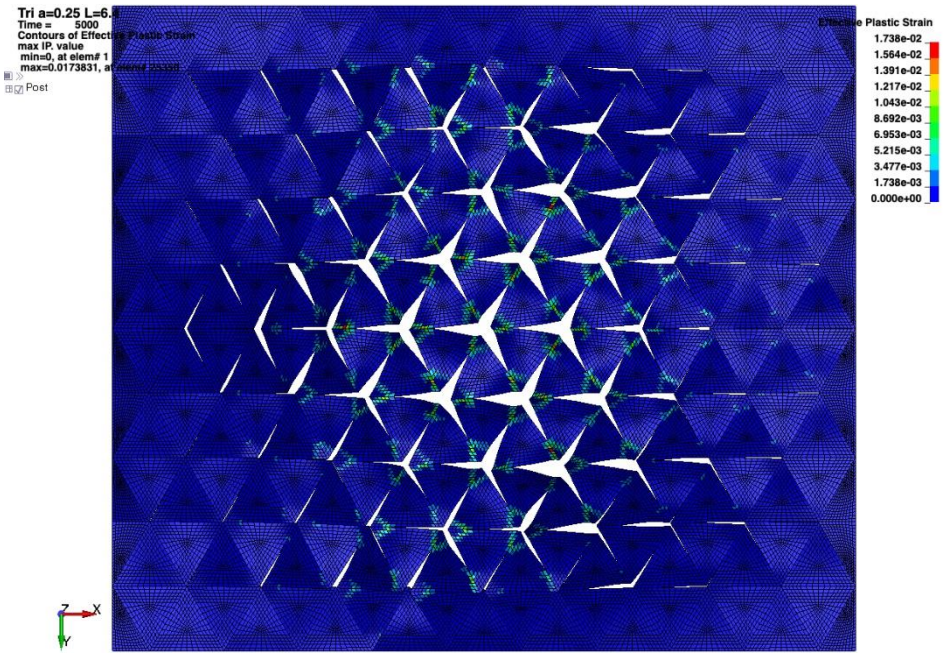

Figure 52. Effective plastic strain in copper foil at indentation of 10 mm, a = 0.25, L = 6.4 mm.

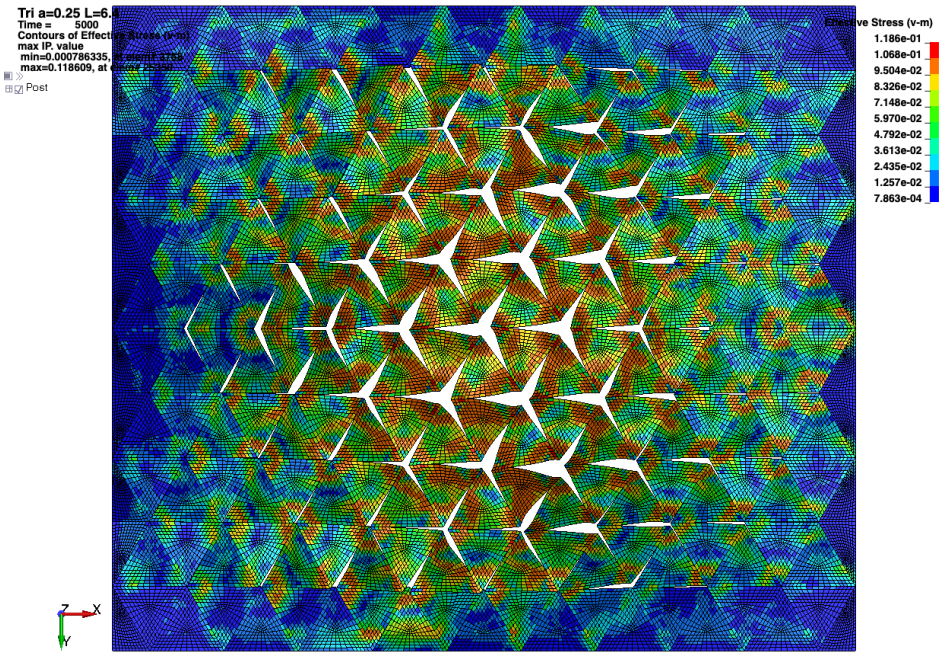

Figure 53. Effective stress in copper foil at indentation of 10 mm, a = 0.25, L = 6.4 mm.

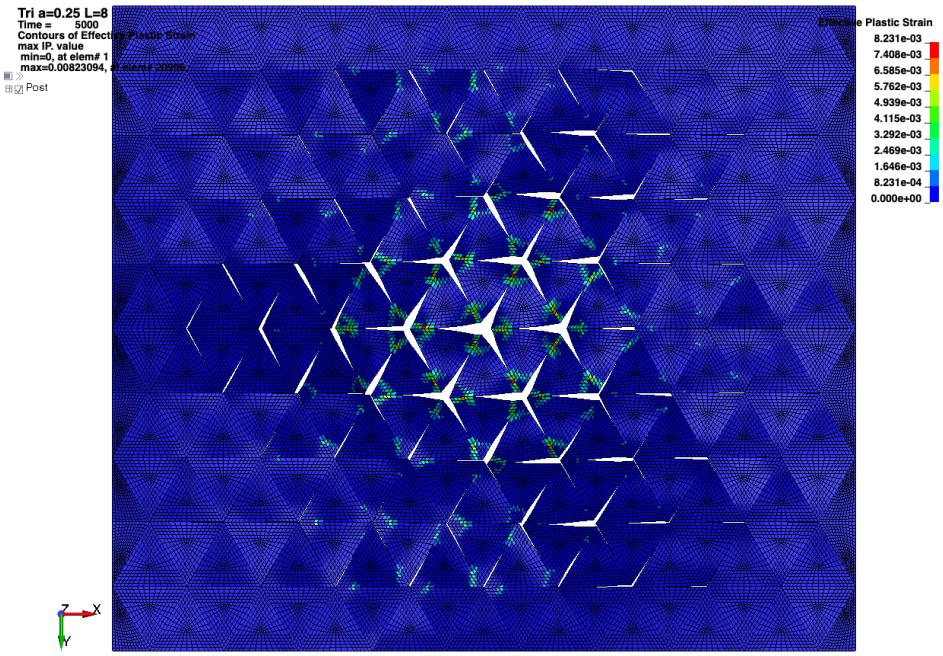

Figure 54. Effective plastic strain in copper foil at indentation of 10 mm, *a* = 0.25, *L* = 8 mm.

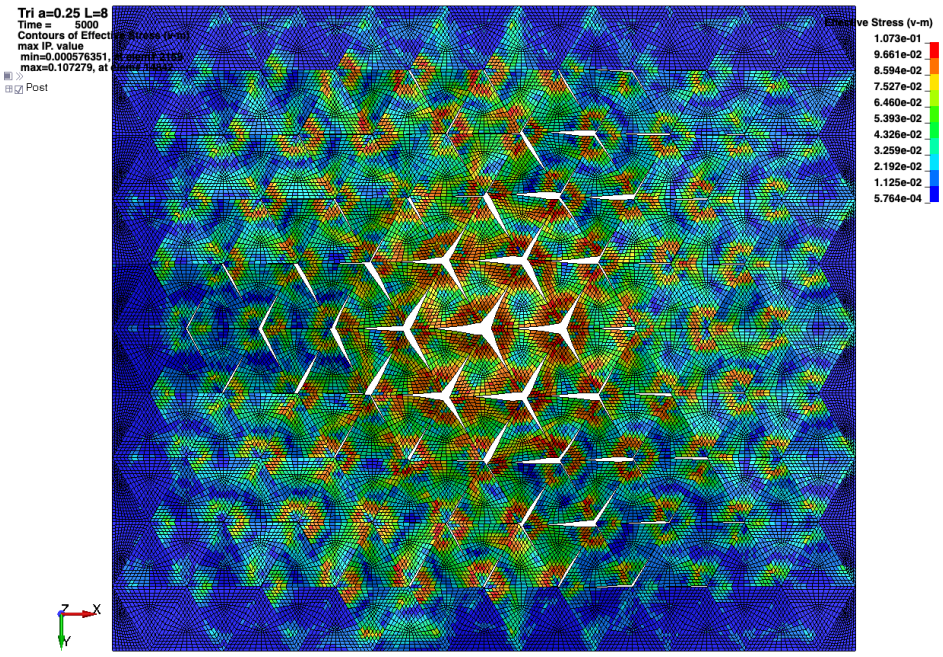

Figure 55. Effective stress in copper foil at indentation of 10 mm, *a* = 0.25, *L* = 8 mm.

The two perforation topologies—rectangular and triangular—have distinctive characteristics. For the same parameters *L* and *c*, triangular perforation has more free edges and therefore will be more pliable to deformation. The triangular pattern is more isotropic, which can be observed by the deformation bands in three distinct directions compared with two for the rectangular pattern. For the same indentation, the rotation of the unit triangles is larger for the triangular pattern compared with the squares in the rectangular pattern, which should lead to more crack propagation and fragmentation. In addition, three fragments must break off to create an isolated patch compared with four in the rectangular pattern. Tearing should theoretically be easier for the triangular pattern. Reducing the relative size of the ligament,

$a = c/L$, and reducing the size of the unit cell, L, should promote fragmentation, although the parameters have to be balanced with the practicality of perforation and handling of the foils during manufacturing.

In summary, models were developed for analysis of thin foil perforation due to in-plane induced tensile deformation. The proposed perforation patterns result in favorable deformation kinematics that would drive simultaneous tearing and fragmentation in the foils. The foil in-plane deformation has essentially only one global degree of freedom, which induces rotation of the connected foil patches, thereby concentrating stresses in the perforated crack tips. This stress concentration is expected to drive tearing cracks in the foil and disassociate the foil patches from the connected foil. The stresses for tearing cracks were directed toward free surfaces, which attract cracks and promote fragmentation. To account for tearing crack propagation and segment fragmentation, tearing models would have to be developed for thin foils, and the relevant driving phenomena would have to be characterized. Such efforts are outside the scope and resources of this study. The practical patterns will likely have unit cells of approximately 8 mm and relative ligament sizes of 0.2.

4.2 TEMPERATURE DISTRIBUTION VIA SIMULATION

A 3D model was developed of the multilayered, stacked, electrode-coated foils in z fold configuration to study the electrochemical and thermal performance of the novel designs that enhance safety and avoid thermal runaway during mechanical impact. For the electrodes, a dual-coated lithium nickel manganese cobalt oxide (NMC) 532 cathode and a graphite anode were considered; the corresponding material parameters are listed in Table 1. The details of the electrochemical model can be found elsewhere [12].

Table 1. Parameters for the electrode materials

Parameter	Description	Unit	Cathode (NMC 532)	Anode (graphite)
D_s	Diffusion coefficient	m^2/s	$3 \cdot 10^{-15}$	$5 \cdot 10^{-14}$
σ	Electric conductivity	s/m	0.04	100
c_s^{max}	Maximum concentration	mol/m^3	49,500	30,000
c_s^0	Initial concentration	mol/m^3	17,820	29,670
α_a	Anodic transfer coefficient	—	0.5	0.5
α_c	Cathodic transfer coefficient	—	0.5	0.5
k	Reaction rate constant	$A \cdot cm^{2.5}/mol^{1.5}$	0.23327	0.4854
t_+^0	Transference number	—	0.462	0.462
R_{film}	Film resistance	$\Omega \cdot m^2$	0.014	0.025
ε_e	Volume fraction of liquid	—	0.331	0.351
ε_s	Volume fraction of solid	—	0.560	0.521
ε_f	Volume fraction of filler	—	0.108	0.128
R_s	Particle radius	m	$1 \cdot 10^{-6}$	$2.5 \cdot 10^{-6}$
p	Bruggeman constant	—	2.0	2.7

For the baseline study, the authors simulated the coupled electrochemical and thermal performance of the pouch cell discharged under constant current condition. The pouch cell dimension was 24 × 16 × 0.4 cm. The heating within the cell, in addition to electrical work, was attributed to electrochemical reactions. The heat associated to electrochemical reactions can be broken down to the heat generation that consists of irreversible energy loss due to cell polarization, reversible entropy changes due to half-cell reactions, and ohmic heating within the cell sandwich. The face boundaries of the pouch are subjected to convective

cooling, and the remaining surfaces are assumed to be in adiabatic conditions. Figure 56 shows temperature maps of the cell along the surface and internal to the pouch at the end of discharge at 1C with a lower cutoff voltage of 2.5 V, indicating that the maximum temperature is in the core of the cell and generating thermal gradients along the thickness direction.

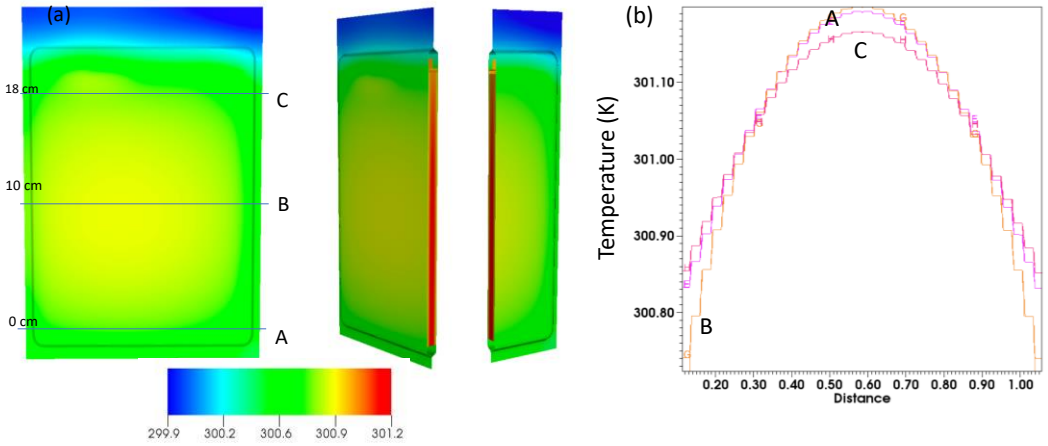

Figure 56. (a) Temperature (K) maps of pouch cells at the end of discharge and (b) lineouts of temperature profiles along the thickness at three different heights of the cell.

To further analyze the temperatures, the lineouts of the temperature profile along the thickness at three different heights of the cell are plotted in Figure 56(b). This 2D plot indicates that although gradients exist along the thickness, there is uniformity and only minor variations along the height of the cell.

Also, the 2D slices of the temperature were plotted at three discrete locations (Figure 57) along the thickness of the cell to show the uniformity, indicating that the cell does not have any heterogeneity.

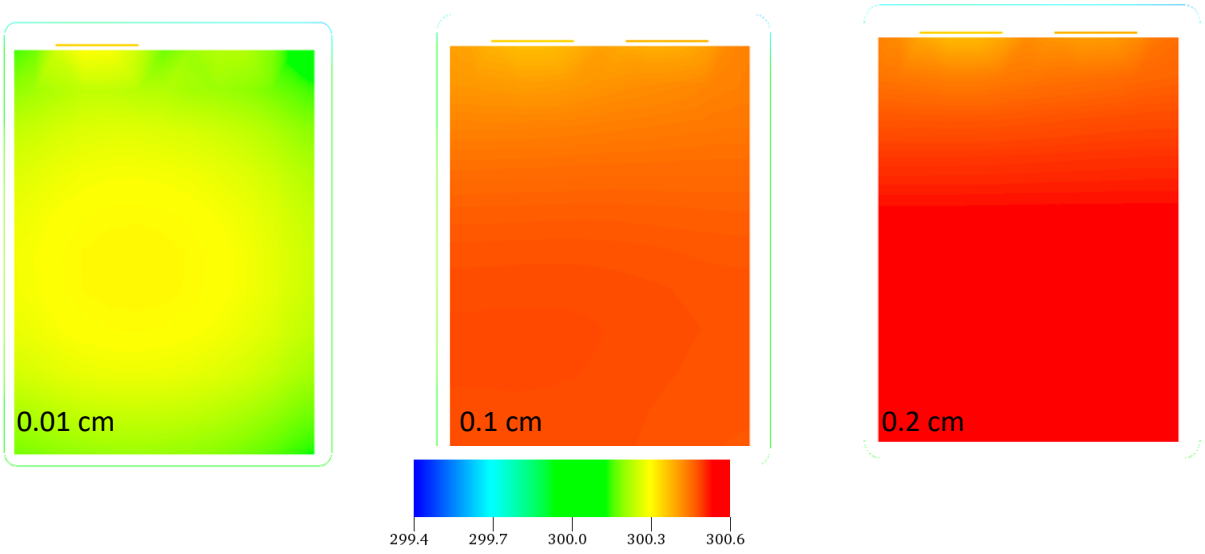

Figure 57. Temperature distribution at various locations from the surface of the pouch cells.

Similar to the baseline study, the electrochemical and thermal model was used to simulate the pouch cell with slitted electrodes, which are known to improve safety when subjected large deformations based on structural mechanics simulations. The design pattern of the slits for the electrodes are such that when the

cell is subjected to large deformations through thickness, the predefined tear would expand and electrically isolate the electrodes, causing smaller or no shorts and thus avoiding thermal runaway. These designs, as shown in Figure 58, need to be evaluated for electrochemical and thermal performance to determine if they cause any inhomogeneity.

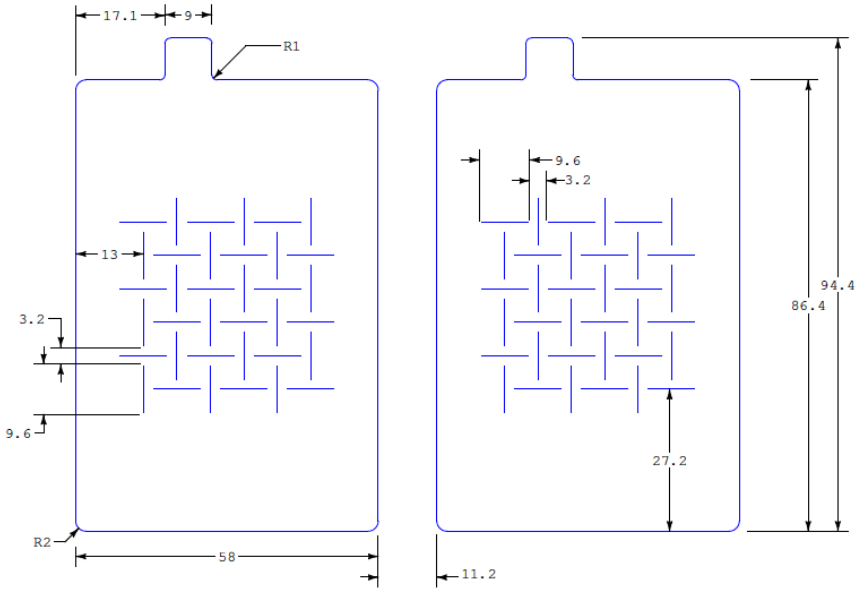

Figure 58. Slitted patterns applied to electrodes for improved safety.

The slitted pattern electrodes were constructed for both cathode and anode and were dual-coated and used in the pouch cell. Figure 59(a) shows the temperature distribution at the end of the constant current discharge at 1C with a lower cutoff voltage of 2.5 V.

The lineout plots (Figure 59(b)), as noted previously, are along the thickness direction at three different heights. This plot shows that the temperature profile varied significantly along the height of the cell, indicating that the slitted patterns introduce heterogeneity. The likely cause of the inhomogeneous behavior could be increased heat flux through the neck of the slitted patterns. The intention of the patterns is to generate isolated regions during deformation, but under normal operation, the patterns are supporting contiguous regions of heat flow and causing localized heating, which introduces gradients in the vertical direction.

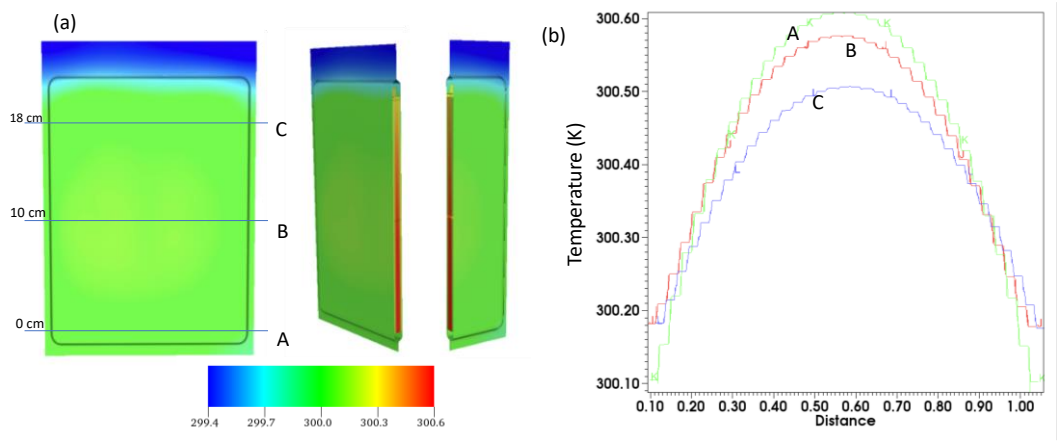

Figure 59. (a)Temperature (K) maps of pouch cells with slitted electrodes at the end of discharge and (b) lineouts of temperature profile along the thickness at three different heights of the cell.

To understand this more, Figure 60 shows the 2D slices of the electrodes along the cell depth at three discrete locations. Compared to the baseline study, we see more predominant temperature gradients along the height of the cell combined with the gradients along the thickness direction.

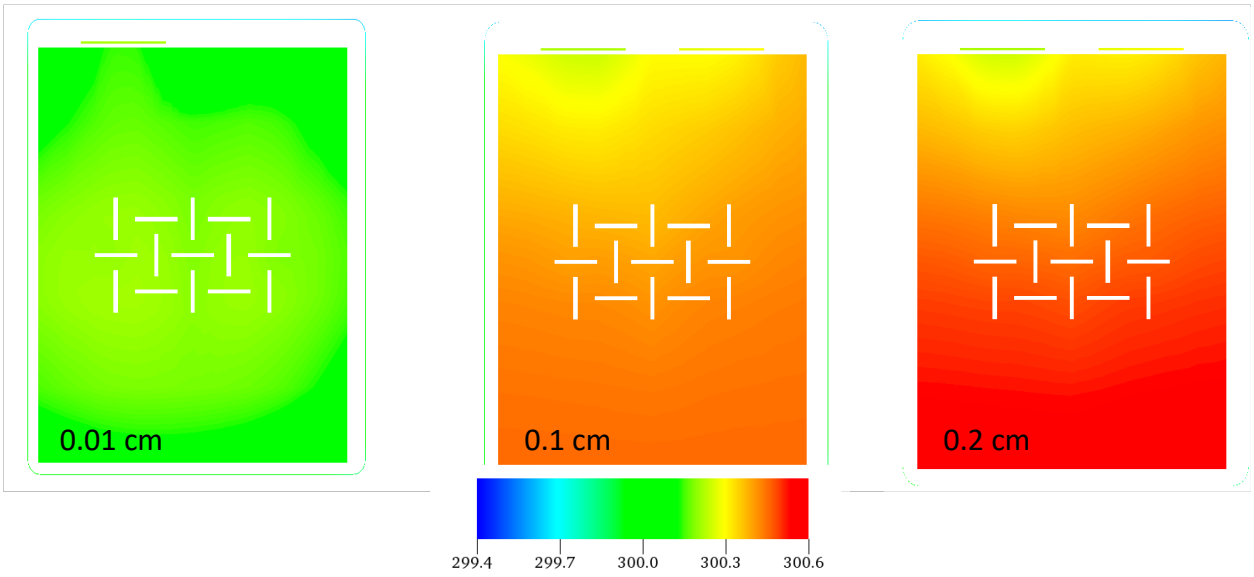

Figure 60. Temperature distribution at various locations from the top surface of the pouch cells.

4.3 ELECTRODE FABRICATION, POUCH CELL ASSEMBLY, AND CELL PERFORMANCE

The cathode and anode were coated using a pilot-scale slot-die coater at ORNL's BMF. The cathode consisted of $LiNi_{0.6}Mn_{0.2}Co_{0.2}O_2$ (NMC 622), Denka carbon black, and Solvay 5130 polyvinylidene fluoride in a 90/5/5 weight ratio. The anode consisted of graphite (SLP1520 P), carbon black (super P C65), and Kureha 9300 polyvinylidene fluoride in a 92/2/6 weight ratio. Both anode and cathode were coated on conventional metal foils and metallized polymer films, respectively. Both electrodes were calendered to ~35% porosity. The areal loadings of the cathode were 3 mAh/cm^2, and of the anode were 3.3 mAh/cm^2. Four types of cells were assembled into 1 and 5 Ah pouch cells. The cell conditions are listed in Table 2. Figure 62 shows some 1 Ah pouch cells.

Table 2. Four types of pouch cells

Cell label	Current collector	Slitted electrodes (yes/no)
BL	Aluminum and copper for the cathode and anode	No
BL_slit	Aluminum and copper for the cathode and anode	Yes
MP	Aluminum-PET and copper-PET for the cathode and anode	No
MP_slit	Aluminum-PET and copper-PET for the cathode and anode	Yes

PET: polyethylene terephthalate

Figure 61. Images of 1 Ah pouch cells.

The pouch cells went through four cycles at a 0.1C charge and discharge rate as formation before being subjected to long-term cycle testing at a C/3 charge and discharge rate, and rate performance testing with a C/3 charge rate and various discharge rates. The voltage window was between 3.0 and 4.2 V. As shown in Figure 62(a), all cells exhibited approximately 1 Ah initial capacity, and the cells with slits showed slightly lower capacity owing to loss of materials when creating slits. In general, all four types of cells demonstrated good cycle life, and the cells without slits were slightly better. This indicates that replacing metal foils with metallized polymer as the current collector does not affect the cell cycle life at relatively low current density. This was confirmed by the rate performance, as shown in Figure 62(b). All four types of cells showed identical rate performance (normalized capacity) up to C/2. The rate performance started deviating at 1C, where the addition of slit patterns lowered the capacity.

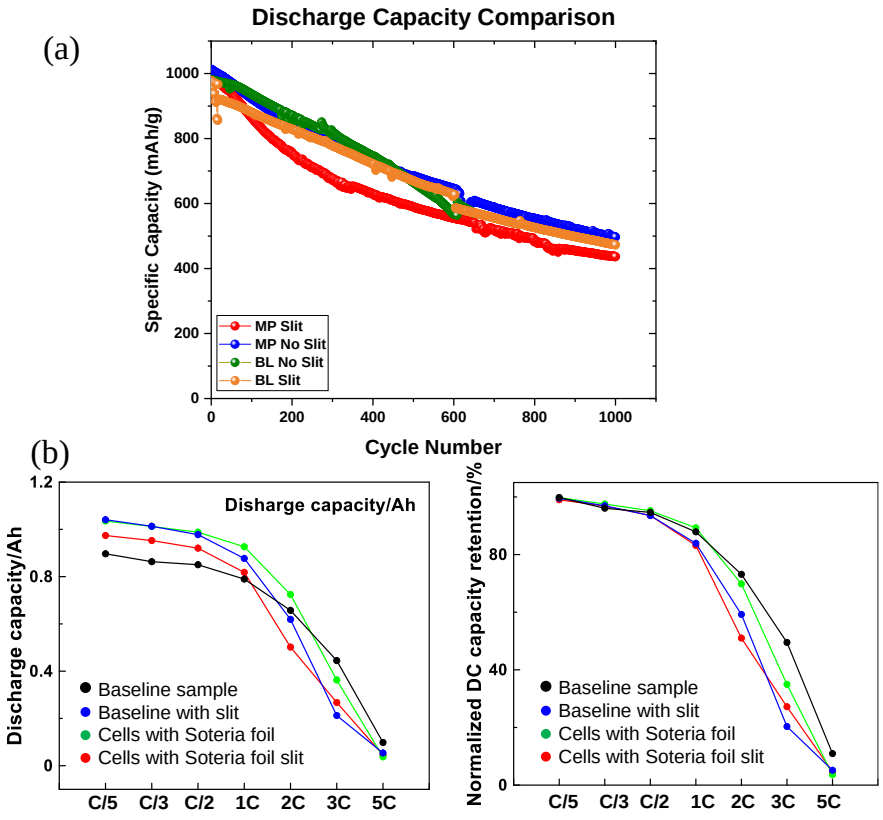

Figure 62. Electrochemical performance of 1 Ah pouch cells—(a) 1,000 cycles at a C/3 charge and discharge rate and (b) rate performance at a C/3 charge rate and various discharge rates.

4.4 THERMAL RUNAWARY EVALUATION TCF PROJECT SUMMARY: THERMAL RUNAWAY TESTING

The concept of reducing volume surrounding the short-circuit location during deformation of LIBs was investigated experimentally. It is well-documented that small-capacity cells of the same cathode chemistry are less likely to go to thermal runaway than large-capacity cells. Meanwhile, for the same cells, the higher the state of charge (SOC), the higher the risk of thermal runaway. By disconnecting the area experiencing short circuit, local current can be controlled, and the Joule heating will not result in rapid temperature rise reaching the onset of exothermic reactions. Three approaches were used to demonstrate the effectiveness of minimizing thermal runaway risk:

1. Slitted electrodes were made at the BMF. Cells of 1 Ah NMC were assembled and compared with baseline cells.

2. Double indentation: the slitted cells were indented with a large-diameter sphere, followed by an indentation of a small indenter.

3. Cells of 5 Ah NMC using a metallized film current collector (MFCC) were compared with baseline cells.

Mechanically induced internal short circuit by single-side indentation was used to evaluate thermal runaway responses of various cells prepared in this project. A test protocol developed by ORNL and Sandia National Laboratories was used.

4.4.1 LIBs

As shown in Figure 63, two types of cells made at BMF were received for indentation testing.

- Baseline cells: 1 Ah NMC cells (four pairs of electrodes, 1.2 mm thick): 20 cells
- Baseline cells with slits in current collectors: 15 cells
- Cycling: Bitrode cycler
  - Rest → discharge to 3.0 V at 0.5 A → rest → charge to 4.2 V at 0.5 A and constant voltage until 0.025 A
  - Cycle five times to 100% SOC
  - Testing: 100%, 80%, 60%, and 30% SOC

Another set of cells was produced by Soteria. NMC 811 cells were divided into (1) baseline cells with an NMC 811 cathode and graphite anode using traditional current collectors of copper and aluminum; and (2) NMC 811 cells using MFCC.

All the batteries were tested by the single-side indentation method to assess the thermal runaway risk. Destructive and nondestructive examinations using x-ray computed tomography (XCT) were used for postmortem studies.

Figure 63. Baseline and slitted cells (1 Ah) received from ORNL's BMF (left) and Soteria cells (5 Ah) (right).

Test protocols

- Purpose: develop a mechanically induced internal short-circuit test that is sensitive enough to distinguish thermal runaway risks
- Single lithium-ion cells: pouch or prismatic cells up to 33 Ah
- Indentation:
  - Stainless steel sphere or blunt indenter, as shown in Figure 64
  - Radius: 6–8 mm
  - Cell support: stainless steel block
- Loading:

    - Motor-driven or hydraulic load system
    - Speed: 0.01–0.1 in./min (0.25–2.50 mm/min)
- Measurements/monitoring: (DAQ rate at 10 Hz or faster)
    - Open circuit voltage: V_{oc}
    - Load
    - Displacement
    - Cell surface temperature (next to the indenter) and multiple points on the surface, temperature on positive/negative tabs measured by thermocouples or IR imaging
- Short-circuit detection and post-triggering actions:
    - Voltage drop $V_{oc} \geq 100$ mV
    - Indenter to retract at 10× speed or stay in place for 15 min
    - Keep recording V_{oc}, temperature, load, and displacement for 5 min

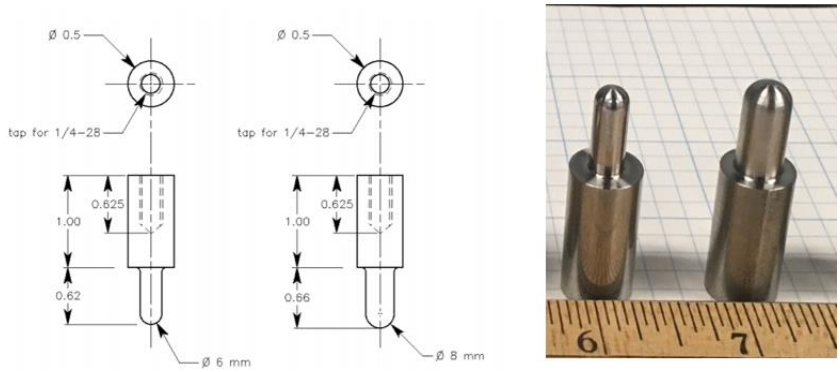

Figure 64. 6 mm and 8 mm indenter designs and machined stainless steel indenters.

Test results: slitted cells

The following test results are for the baseline and slitted cells.

Baseline NMC 1 Ah cells

BMF NMC cell conditioning was performed with four cycles to determine the actual cell capacity. The cells were discharged to the planned SOC. Indentation tests were carried out after cycling. The test setup is shown in Figure 65. A servo motor–driven load frame was used for indentation. The motion was controlled by a LabView program that also collects load, displacement, and voltage vs. time data. The cell temperature was recorded by thermocouple(s) from a separate National Instrument temperature module or from an FLIR A325 camera. The small chamber (1 × 1 × 2 ft) was used to test cells up to 3 Ah, and a larger chamber (20 × 10 × 5 ft) was used to test cells up to 35 Ah. As expected, all the baseline 100% SOC cells went to thermal runaway. However, a slitted cell did not go to thermal runaway.

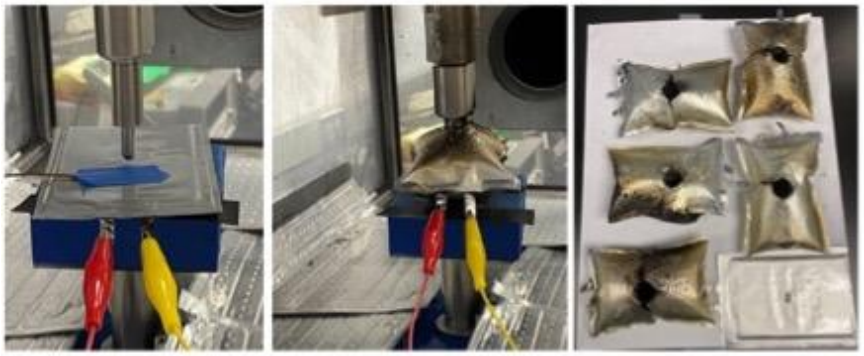

Figure 65. Indentation test of slitted and baseline 1 Ah cells: test setup and cell with and without thermal runaway.

Figure 66 shows baseline cell #1 had a voltage drop accompanied by a decrease in compressive load, and the cell temperature increased 2°C–3°C initially. This was followed by another delayed voltage drop (15–20 s later) and a sharp increase in temperature to 40°C, indicating the onset of thermal runaway. When a thermal runaway is triggered, there is immediate gas generation inside the cell, which causes the pouch to puff up, creating a large gap between the electrodes and the pouch. The thermocouple was taped next to the indenter, and it got loose or detached, which made temperature readings after pouch swelling unreliable. As shown in Figure 67 and Figure 68, the thermocouples were in contact a little longer and a temperature rise to 160°C–180°C was detected.

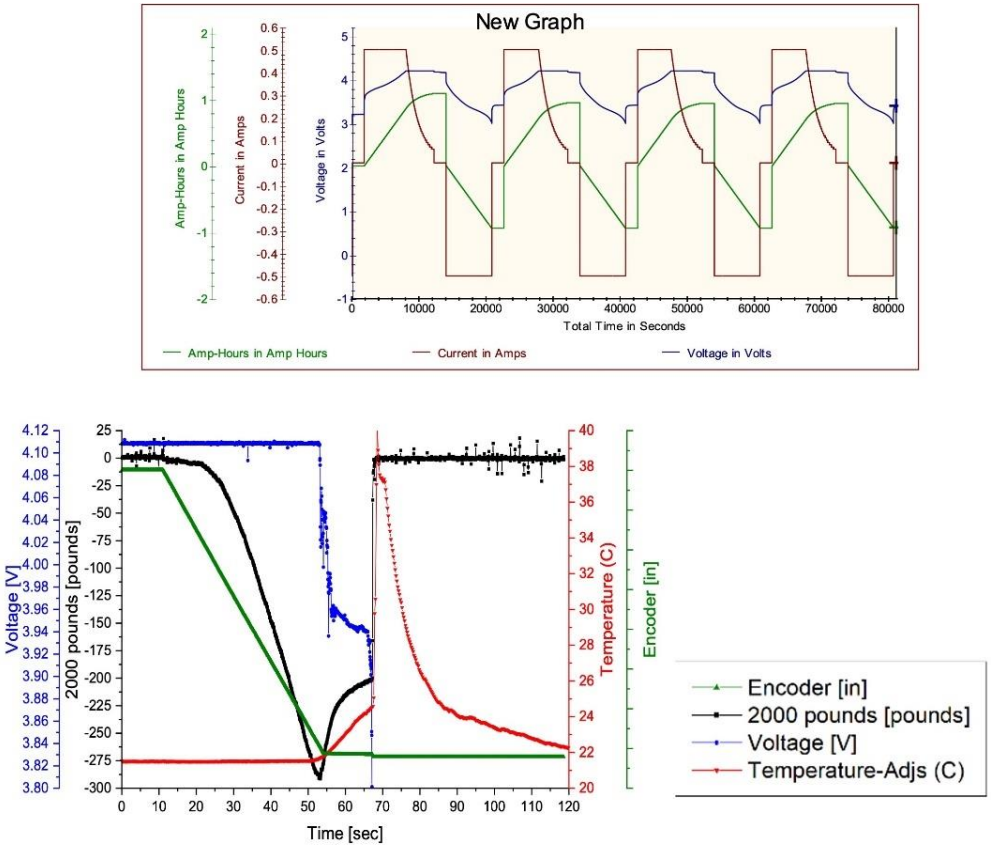

Figure 66. NMC cell #1: cell conditioning plots and indentation test results.

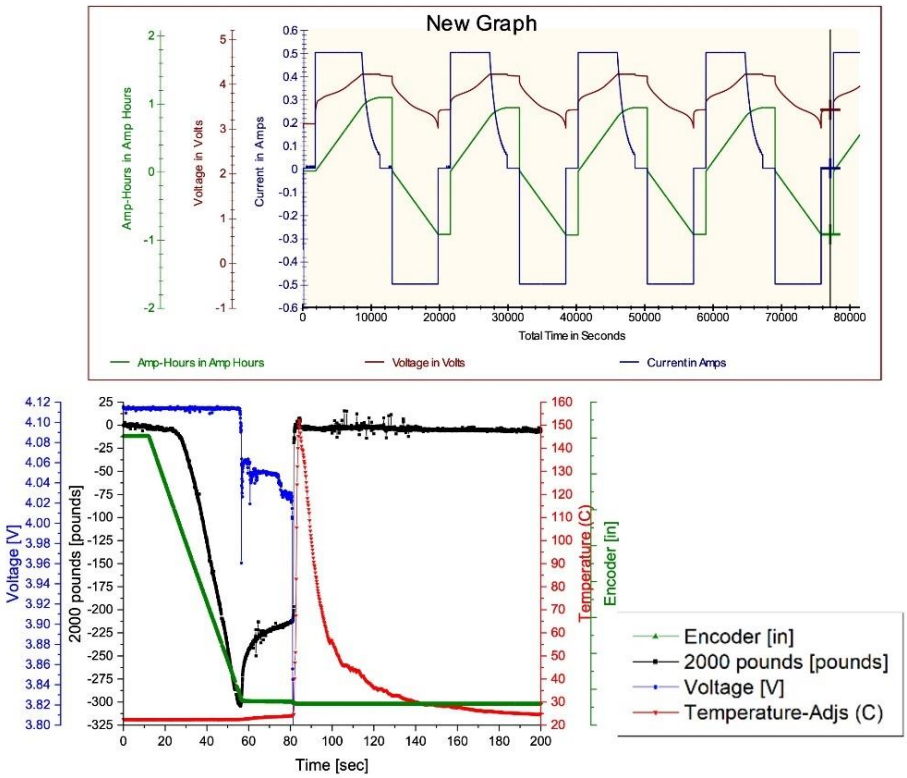

Figure 67. NMC cell #3: cell conditioning plots and indentation test results.

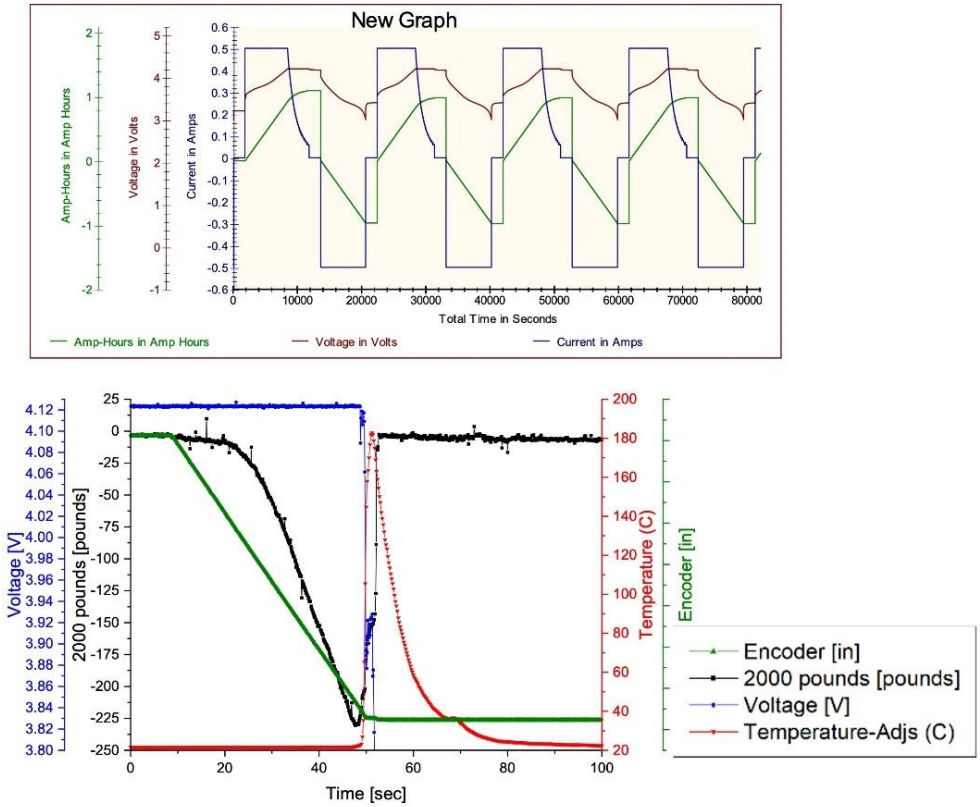

Figure 68. NMC cell #6: cell conditioning plots and indentation test results.

Slitted NMC 1 Ah cells

NMC cells with slits on electrodes were tested under the same conditions. The results were mixed. Figure 69 shows that one slitted cell went to thermal runaway because the indentation was not stopped owing to the voltage detection error and thermocouple detachment. Thermal runaway was captured by the rapid temperature rise. When the voltage drop was properly detected, as shown in Figure 70, the maximum load was approximately 250 lb and temperature increase stayed below 30°C with a slow rate.

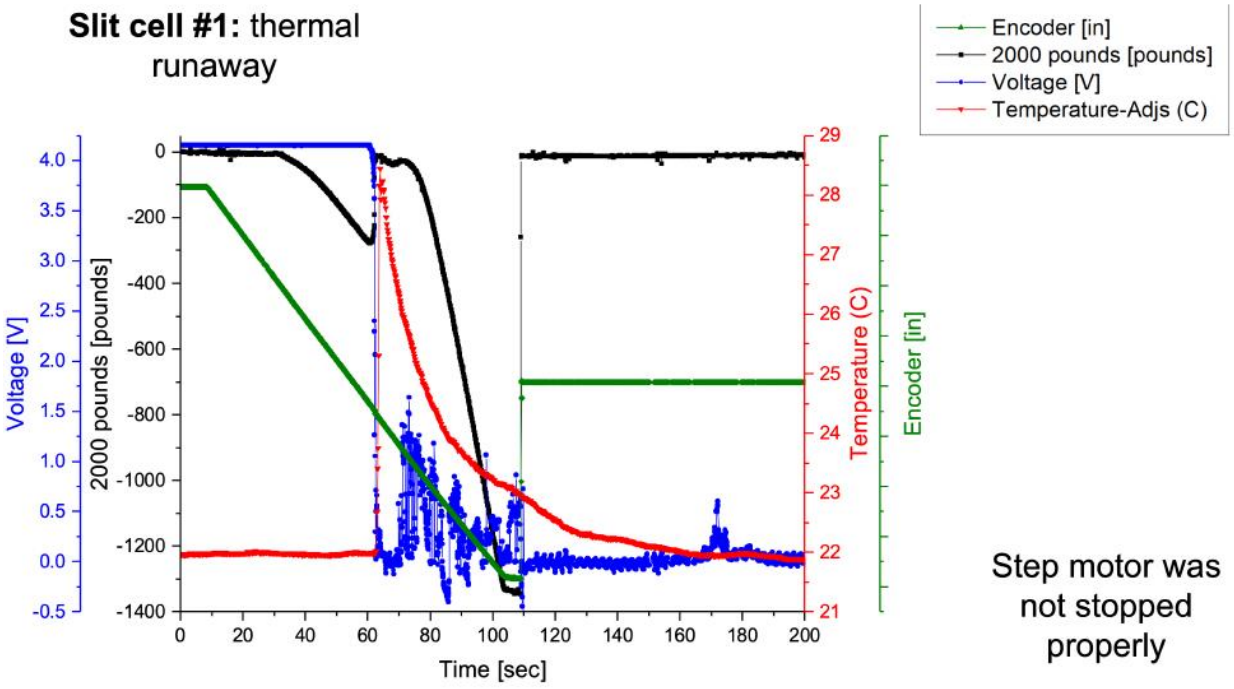

Figure 69. Slitted cell #1: thermal runaway due to over-indentation.

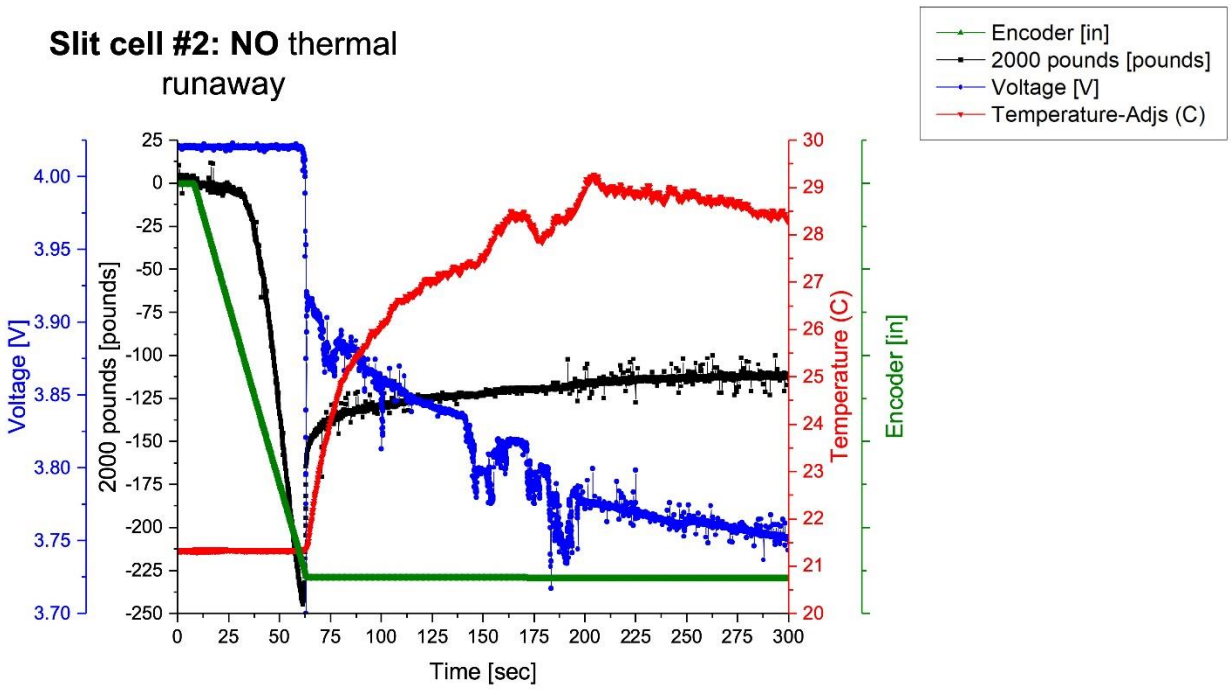

Figure 70. Slitted cell #2: no thermal runaway.

Figure 71 shows a slitted cell that went to thermal runaway. The maximum load was approximately 275 lb and the thermocouple was intact until 160°C. The main reason for the inconsistency was the size of the indenter (6 mm) and the spacing of the slits (>10 mm). Because the total cell thickness (including the pouch) was <2 mm, there was not enough room for deformation, and the slits did not detach into smaller pieces as intended. However, the spacing of the slits could not be smaller because of tool limitations and assembly requirements.

Figure 72 shows the initial cycles of the slitted cells, which were very consistent for most of the cells.

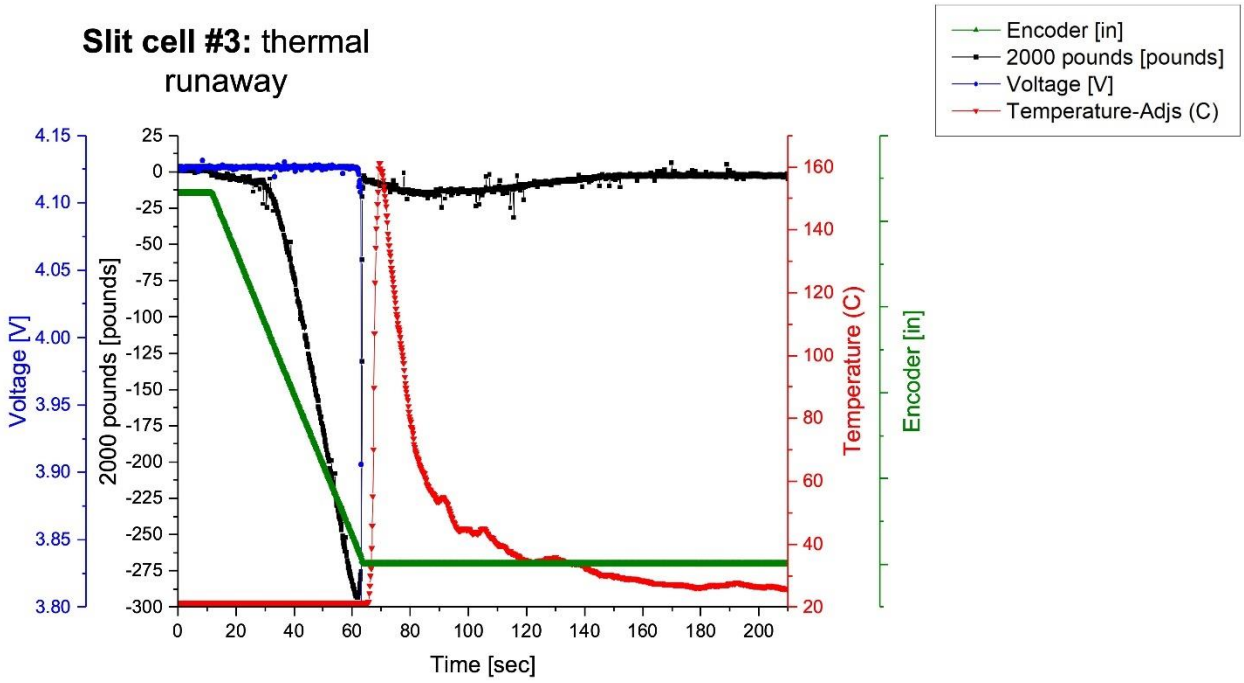

Figure 71. Slitted cell #3: thermal runaway.

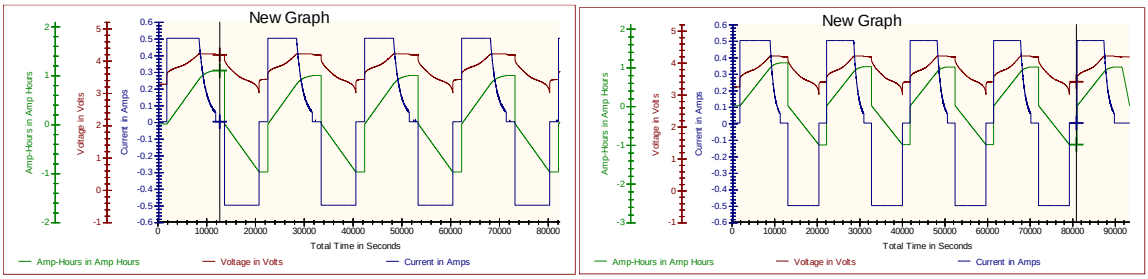

Figure 72. Cycling of NMC 1 Ah slitted cells.

Double indentation of slitted cells

Based on the simulation of slitted cells, the deformation area (or the indenter diameter) should be much larger than the slit spacing. Using a 6–8 mm indenter resulted in inconsistent results because the indenter must be positioned at the correct location to break up the cell into smaller units. To simulate this condition, a larger-diameter sphere (2 in. [25.4 mm] in diameter) and a dry cell were used, as shown in Figure 73. Five foam pads from a Chevy Volt (2017) battery pack were stacked together and taped to provide extra cushion. The indentation was more than 7 mm deep. Figure 74 shows the cell and inside layers after indentation. Because of the foam layers, the cell was deformed beyond its thickness. However, the cell was wrinkled because the top surface was not restricted. Therefore, the slitted cathodes and anodes did not break apart.

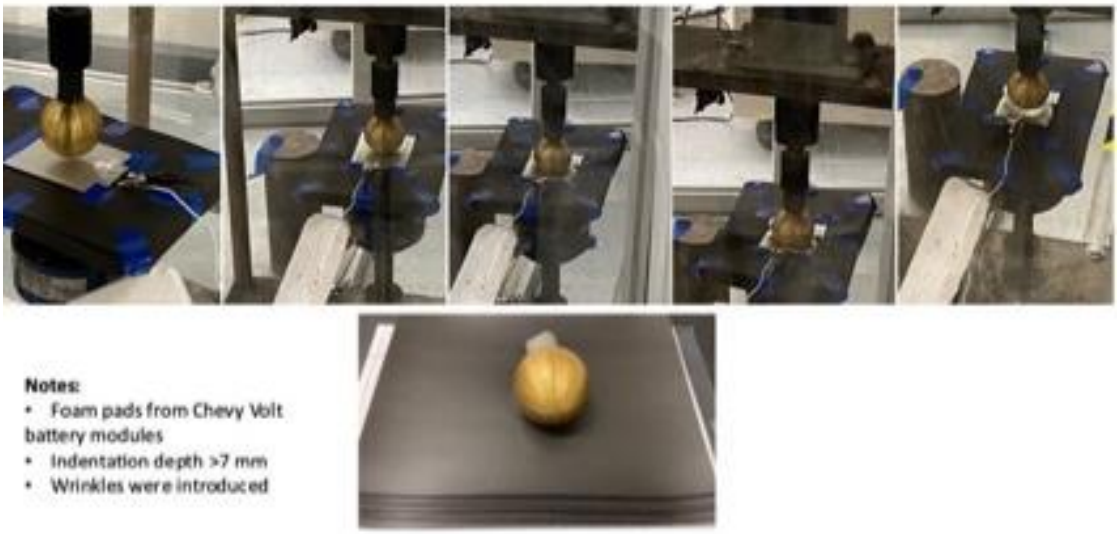

Figure 73. Indentation with 2 in. (25.4 mm) diameter sphere and five foam layers.

Figure 74. A slitted dry cell after indentation, and cell components.

To improve the top surface restriction, a polymer plate from a Nissan Leaf (2013) battery pack was used, as shown in Figure 75. The middle of the plate had a circular opening to allow the 2 in. (25.4 mm) diameter sphere to come through. The top plate was taped to the five-layer foam pads. As shown in Figure 75, the electrode tabs were exposed to allow detection of short circuit. The results demonstrate that the cell was wrinkled again because the pouch was separated from the top plate. The picture of an anode (coated on one side) shows that the slits were stretched but did not separate.

Finally, a Nissan Leaf plate was used without an opening. The cell was also taped to the foam pads. As shown in Figure 76, after indentation, the cell showed less severe wrinkling. Both the anode and cathode showed large openings, as well as tearing of the slits. The separator also showed damage (a small area was stretched and became clear) by the shear of the electrodes.

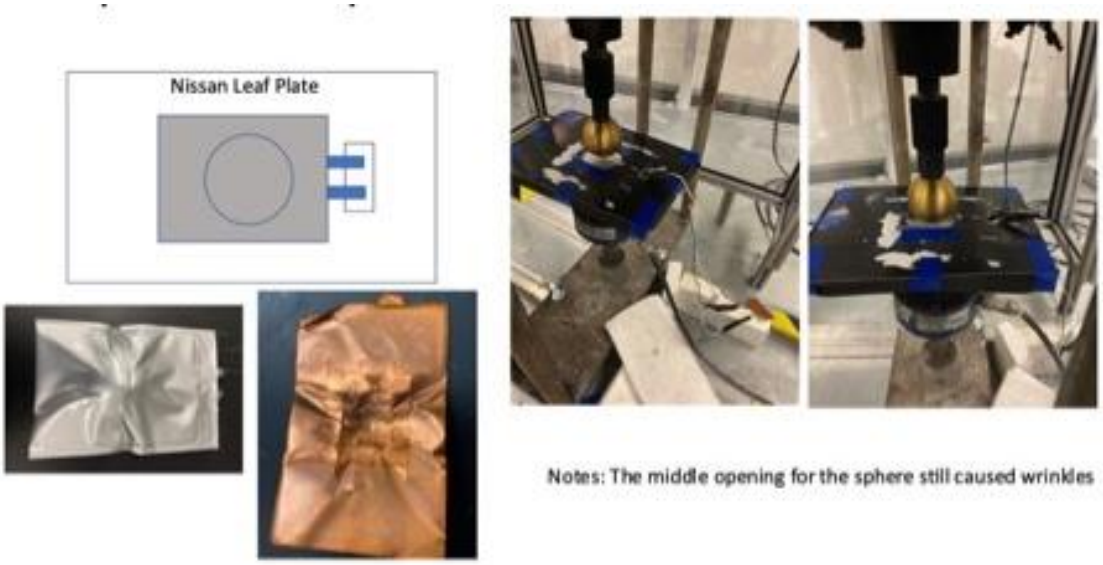

Figure 75. Using a Nissan Leaf polymer plate with a center hole.

Figure 76. Using a closed Nissan Leaf top plate, and the slits opened up.

Inducing short circuit using a 2 in. (25.4 mm) diameter sphere requires more than 2,000 lb of force, and the deformation would be extremely large and would exceed practical conditions in a battery pack. A

second indentation was performed after the 2 in. (25.4 mm) indentation, as shown in

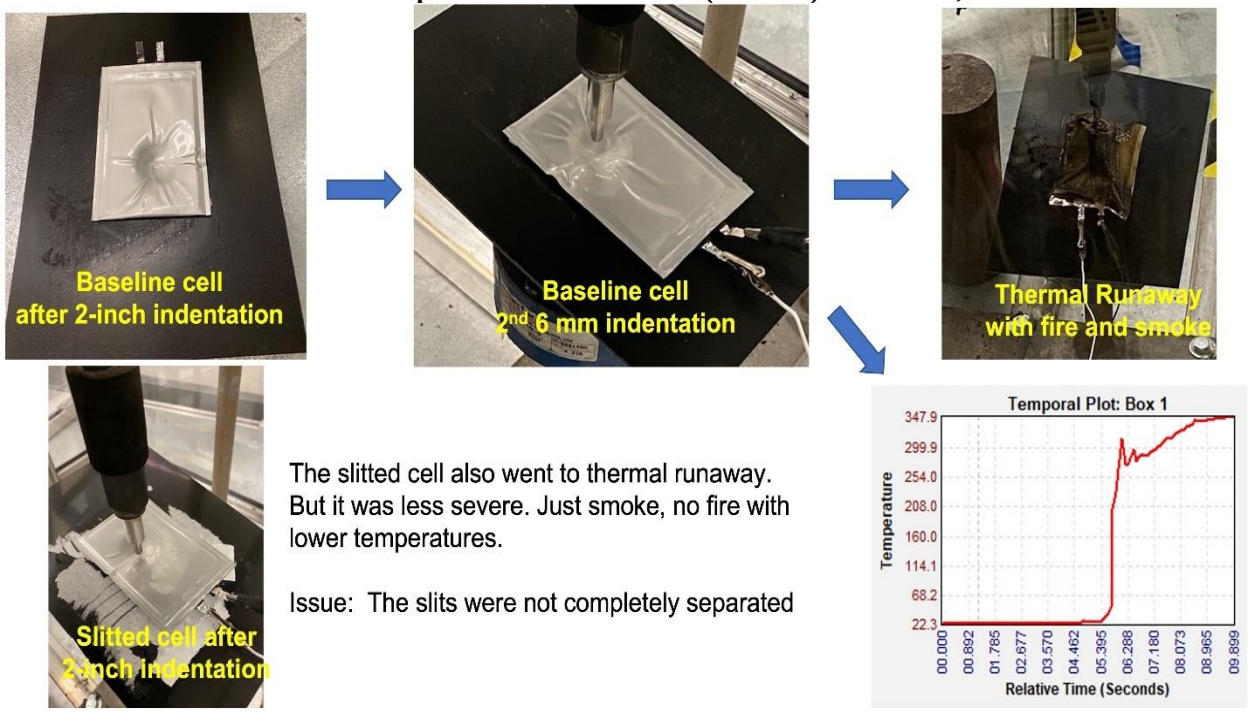

Figure 77, using a 6 mm diameter indenter. The result was a thermal runaway with temperatures (recorded by the IR camera) exceeding 348°C. The thermal runaway was triggered because complete separation of the slitted area was not achieved. However, the force required to trigger thermal runaway was more than 50% more for the slitted cell compared with the baseline cell, as shown in

Figure 78. These experiments demonstrate that breaking up the slitted electrodes in a cell requires perfect contact among cells and may be achieved in a cell stack. In a practical cell pack, large cell deformation without wrinkling is difficult to avoid. One way to improve the chance of break up is to reduce the size and spacing of the slits.

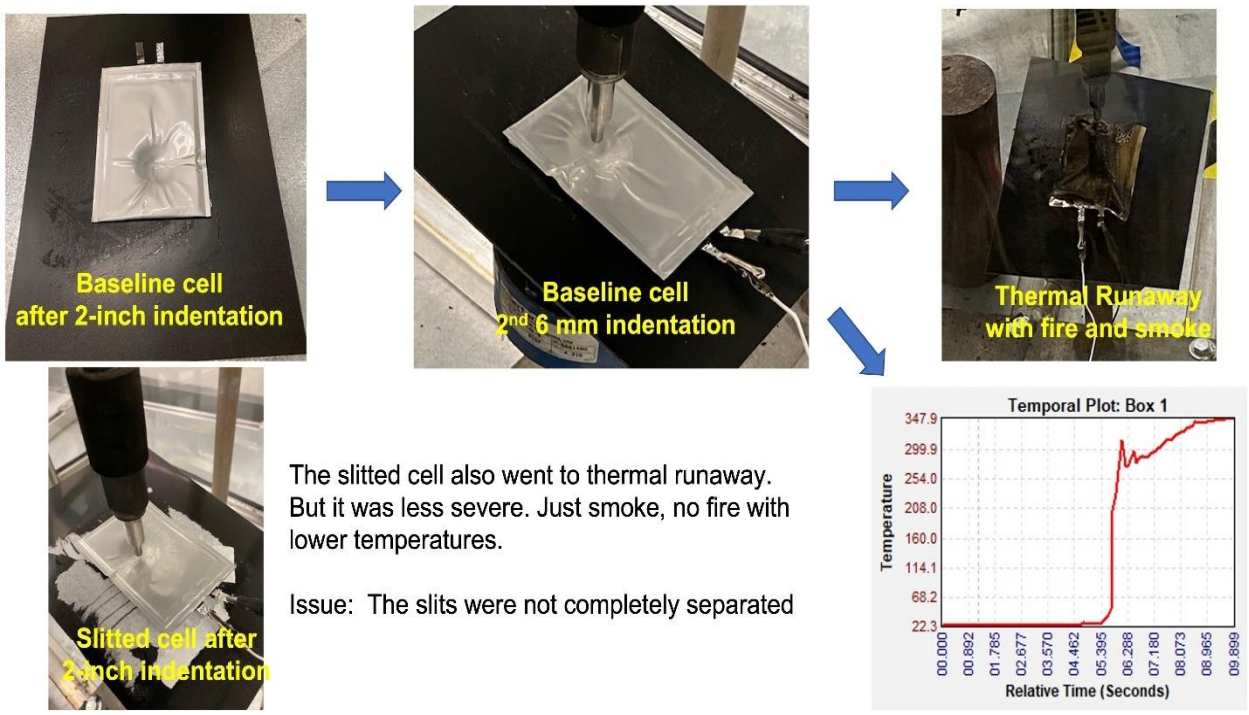

Figure 77. Double indentation on a slitted cell.

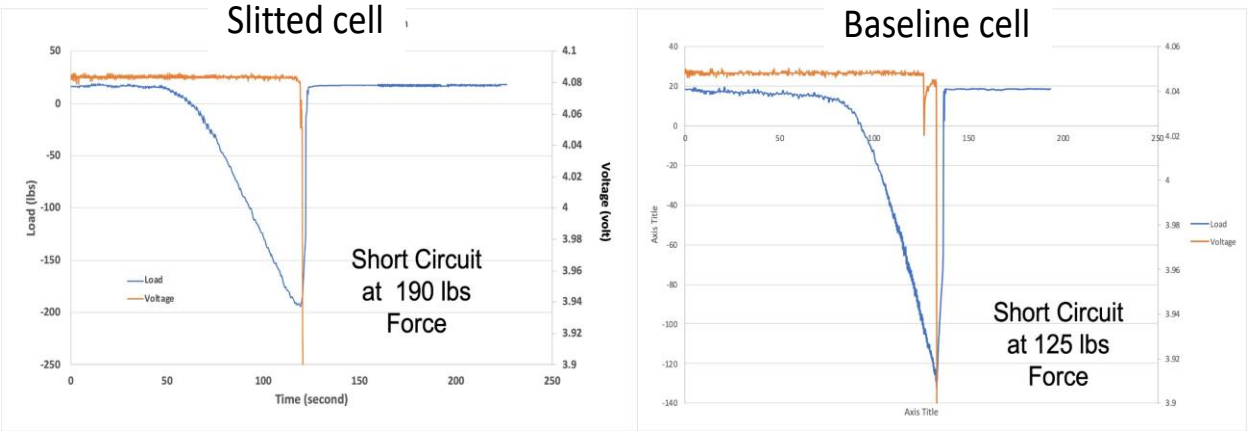

Figure 78. Comparison between the force required to induce thermal runaway in baseline and slitted cells using double indentation.

Cells with metallized polymer current collectors

This section compares the cells with electrodes coated on conventional metal foils and metallized polymer films. The mechanical properties of the current collectors were completely changed. The response to indentation also changed. Cells were charged to different SOCs. Table 3 lists 12 control NMC 811 cells and 10 cells with MFCC that were tested. For comparison, test results of 16 lithium iron phosphate (LFP) cells and 14 NMC 532 cells (all with 10 Ah capacity) are also presented.

Table 3. List of tested cells

Cell name	Chemistry	Capacity (mAh)	Sample number
Control NMC	$LiNiMnCoO_2$ (811)	5,200	12
MFCC NMC	$LiNiMnCoO_2$ (811)	5,200	10
Commercial LFP	$LiFePO_4$	10,000	16
Commercial NMC	$LiNiMnCoO_2$	10,000	14

Figure 79(a), (b), and (c) show the NMC 811 control cells, NMC 811–MFCC cells, and 10 Ah LFP and NMC 532 cells, respectively. The NMC 811 control cells went to thermal runaway when the SOC was above 50%. Meanwhile, none of the MFCC cells went to thermal runaway—even with two 100% SOC cells indented using 8 and 12.7 mm diameter indenters. For the 10 Ah NMC 532 cells, all the cells with 60% SOC or higher went to thermal runaway. The 10 Ah LFP cells showed no signs of thermal runaway.

Figure 79. Cells after indentation testing: (a) control NMC 811 cells after testing, (b) MFCC NMC 811 cells, and (c) (top) 10 Ah NMC cells and (bottom) 10 Ah LFP cells.

The simple descriptions of physical and functional effects of thermal runaway were adopted by the battery industry using the European Council for Automotive R&D (EUCAR) thermal runaway severity scores of 0–7, in which 0 represents no effect and 6 and 7 represent fire/smoke and explosion. However, these scores could not distinguish and rank cells effectively.

A new scoring system was developed recently by ORNL and Sandia. Table 4 lists a data-based hazards severity score system based on the 6 mm single-side indentation. Each severity level is associated with a description and a set of specific temperature and voltage criteria. The table is used to distinguish thermal runaway severity. The five levels are similar to the recent multifactor work. However, instead of using terms such as *safe/safety* and *risk*, the definitions are limited to relative severity of thermal runaway under the specific indentation test conditions following the ORNL–Sandia test protocols. The hazards severity levels are very low (VL; 0–10), low (L; 10–25), moderate (M; 25–75), high (H; 75–90), and very high (VH; 90–100).

Table 4. ORNL–Sandia data-based hazard severity levels for single-side indentation

Hazard severity level	Description
1 (VL, 0-10)	Very low: instant local Joule heating, detectable voltage drops
2 (L, 10-25)	Low: localized heating, small voltage drops and recovery
3 (M, 25-75)	Moderate: localized heating spread, significant voltage drops, continued discharge after recovery
4 (H, 75-90)	High: heating due to chemical reactions, cell puff and gas release, voltage drops close to zero
5 (VH, 90-100)	Very high: heating spread to the cell, heavy smoke and possible fire, voltage drops to zero

The hazard severity levels ranging from 0 to 100 are calculated using the following six equations:

$$\text{Severity Level} = \begin{cases} 5, \ if\ Max\ Temperature < 40\ ℃ \\ \min\{ \quad wA * \left(\frac{Max\ Temperature}{160}\right)^{0.25} \\ \quad +wB * \left(\frac{Temperature\ Increase\ Rate}{200}\right) \\ \quad +wC * wCap * wSOC * Voltage\ Drop\ Score \\ \quad +cOffset,\ 100\} \\ 100, \ if\ Max\ Temperature > 160\ ℃ \end{cases} \tag{1}$$

Voltage Drop Score=

$$\begin{cases} 1, \ if\ (Voltage\ Range)/(Initial\ Voltage) < 0.2 \\ 2, if\ \frac{Voltage\ Range}{Initial\ Voltage} > 0.5\ and\ \frac{Final\ Voltage\ Change}{Initial\ Voltage} < 0.2 \\ 3, \ if\ \frac{Voltage\ Drop\ in\ 2\ Seconds}{Initial\ Voltage} < 0.4\ and\ \frac{Final\ Voltage\ Change}{Initial\ Voltage} > 0.7 \\ 4, \ if\ \frac{Voltage\ Drop\ in\ 2\ Seconds}{Initial\ Voltage} \geq 0.4\ and\ \frac{Final\ Voltage\ Change}{Initial\ Voltage} > 0.7 \\ 5, \ if\ \frac{Voltage\ Range}{Initial\ Voltage} > 0.7\ and\ \frac{Final\ Voltage\ Change}{Initial\ Voltage} > 0.7\ and \frac{Voltage\ Drop\ in\ 5\ Seconds}{Initial\ Voltage} > 0.7 \end{cases} \tag{2}$$

$$wA = 2.0*\text{cScale},\ wB = 3.0*\text{cScale},\ wC = 2.0*\text{cScale} \tag{3}$$

$$wCap = \text{Battery Capacity}/10000 \tag{4}$$

$$wSOC = \text{Battery SOC}/100 \tag{5}$$

$$cScale = 95/6,\ cOffset = 5\text{-cScale} \tag{6}$$

Using the data-driven analysis, three major parameters—cell voltage, temperature, and applied indentation load—were considered. Figure 80 shows four typical thermal runaway data sets from the control and MFCC NMC cells with calculated scores of 5.0, 27.1, 60.7, and 100.0, respectively. In the case of severity level = 5.0 (VL) from the MFCC cells with 100% SOC, no significant voltage drop (7–25 mV) was observed during the test, and only a small increase in temperature (from 20°C to 27°C) was detected at about 200 s. The other three levels were from the control NMC cells with SOC of 0%, 45%, and 100%, respectively. The case of severity level = 27.1 (just above L) was with 0% SOC and had a brief voltage drop when the indentation force reached approximately 2 kN, with significant temperature increase (>85°C) detected at the same time. The voltage recovered to above 3 V but dropped slowly to about 0.5 V at the end of the test, and the temperature gradually decreased from 130°C to 30°C. More heat generation was observed in the case with severity level = 60.7 (just above H), which had a longer high-temperature stage (about 150°C from 200 to 800 s). The 45% SOC in the case with security level = 60.7 (H) showed higher energy release as heat than the 0% SOC in the case with security level = 27.1 (M), indicating a positive correlation between severity and SOC. The case with severity level = 100.0 (VH) with 100% SOC detected abrupt changes on both voltage and temperature, which represented a sudden release of energy in accordance with its high severity score. The focus of this study was from ambient to the onset of thermal runaway. The IR camera temperature range was set to have a maximum temperature of 150°C. The maximum temperature after thermal runaway was not tracked closely or used in the calculations. The movement of the pouch and cell after thermal runaway made it difficult to

measure the surface temperature accurately. High sensitivities in temperature and voltage made the severity analysis before the onset of thermal runaway more sensitive in ranking different cells.

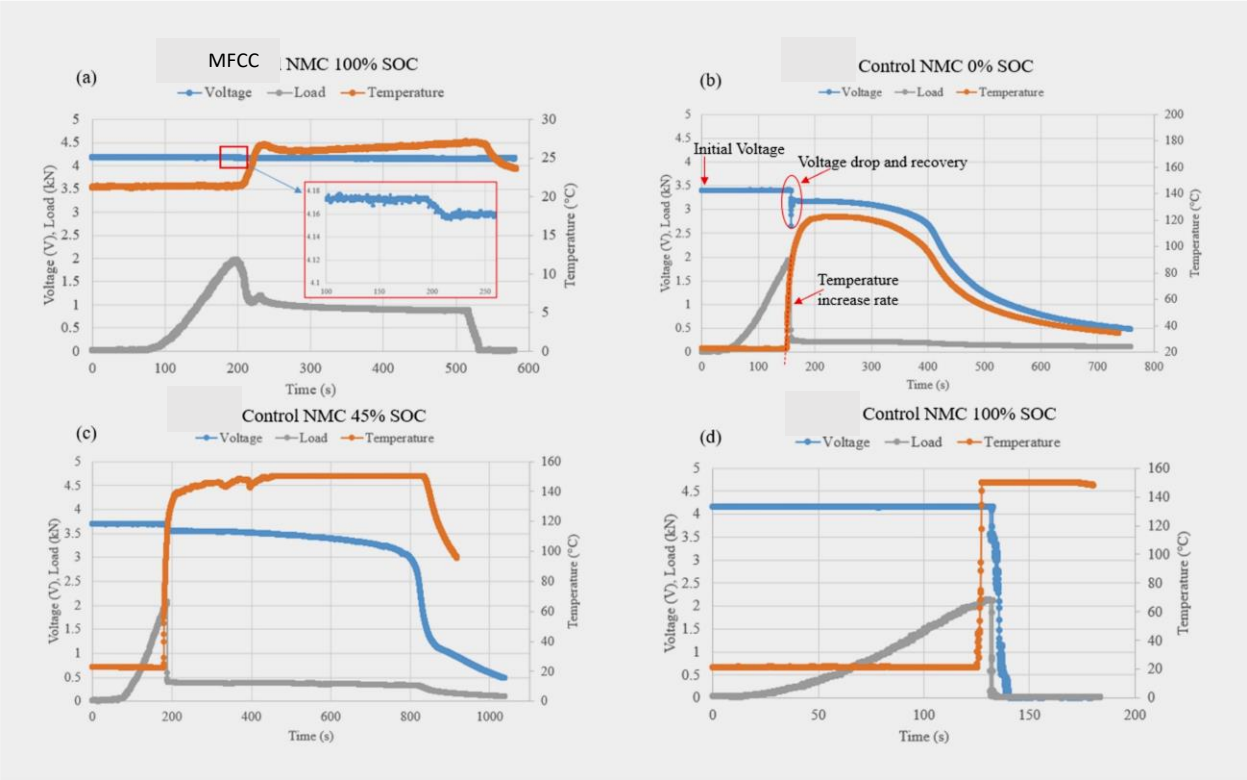

Figure 80. Examples of four thermal runaway severity levels: (a) MFCC NMC 100% SOC with calculated severity level = 5.0, (b) control NMC 0% SOC with calculated severity level = 27.1, (c) control NMC 45% SOC with calculated severity level = 60.7, and (d) control NMC 100% SOC with calculated severity level = 100.0.

Figure 81 depicts the calculated thermal runaway severity in this study. For clarity, the results are presented in two groups: Figure 81(a) shows results for three types of NMC cells, and Figure 81(b) shows the results for 10 Ah LFP cells. The thermal runaway severity clearly divides the cells responses into three regions: (1) the top region (H and VH), which has high or very high potential of thermal runaway, particularly when the cells are fully or close to fully charged; (2) the middle region (M), in which the highest hazard severity level is always below 75.0; and (3) the bottom region (L and VL), which has the lowest severity level. Table 5 also lists the data from the tested cells plotted in Figure 81, with observed severity level and calculated severity level included. Despite using different severity level scales, a good agreement between observed and calculated hazards severity level was reached by using the empirical equations presented in Eqs. (1)–(6) to cover different types of cells and SOCs.

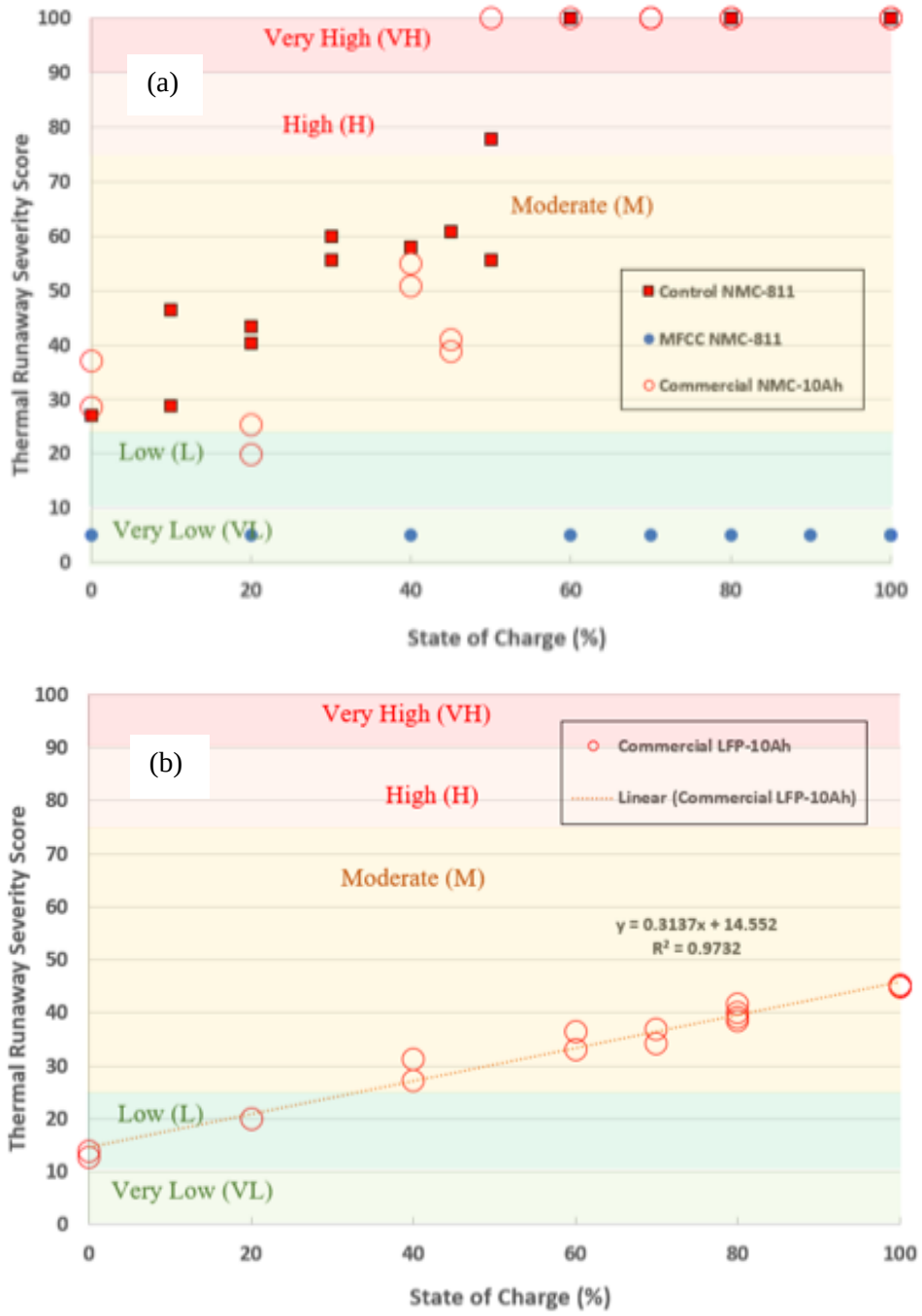

Figure 81. Thermal runaway severity results of three groups of LIBs with (a) NMC cells and (b) LFP cells. The size of the symbols represents the cell capacity.

Table 5. Thermal runaway tests of different batteries, and calculated and observed severity levels

Test name	Calculated severity level (CHS 5–100)	Battery capacity (mAh)	SOC (%)	Observed severity level (OHS)
Soteria-Control-100SOC	100.0	5,190	100	VH
Soteria-Control-80SOC	100.0	4,960	80	VH
Soteria-Control-60SOC	100.0	5,190	60	VH
Soteria-Control-40SOC	57.9	5,190	40	M

Soteria-Control-20SOC	40.3	5,190	20	M
Soteria-Control-10SOC	46.4	5,190	10	M
Soteria-Control-0SOC	27.1	5,190	0	M
Soteria-MFCC-100SOC	5.0	4,960	100	VL
Soteria-MFCC-80SOC	5.0	5,180	80	VL
Soteria-MFCC-60SOC	5.0	5,180	60	VL
Soteria-MFCC-40SOC	5.0	4,720	40	VL
Soteria-MFCC-20SOC	5.0	5,180	20	VL
LFP 10Ah-0SOC	13.8	10,000	0	L
LFP 10Ah-40SOC	27.1	10,000	40	M
LFP 10Ah-60SOC	33.2	10,000	60	M
LFP 10Ah-80SOC	39.2	10,000	80	M
LFP 10Ah-100SOC	44.8	10,000	100	M
NMC 10Ah-0SOC	37.1	10,000	0	M
NMC 10Ah-20SOC	25.3	10,000	20	M
NMC 10Ah-40SOC	55.0	10,000	40	M
NMC 10Ah-60SOC	100.0	10,000	60	VH
NMC 10Ah-80SOC	100.0	10,000	80	VH
NMC 10Ah-100SOC	100.0	10,000	100	VH

CHS—calculated hazardous score; OHS—observed hazardous score

To investigate the internal damage of the MFCC cells, two indentations were made on a cell discharged to 0 V. The cell was cut by a utility knife and taped up to keep the layers in the deformed shape. The small section was investigated using a Zeiss Versa 520 XCT system using a tungsten source running at 140 kV/64.4 mA max (9 W). The data were collected and reconstructed with Zeiss' Scout and Scan software with further analysis conducted on TXM3DViewer. Figure 82 shows the cross-section view of the 2 mm indentation. The two layers were compressed, deformed with some wrinkling, and separated from the indented area. No failure or damage that can cause internal short circuit was detected. As shown in Figure 83, the 3 mm deep indentation caused short circuit. Because the cell had close to zero charge left, no thermal damage was done to the layers. Evidently, the area under the indenter broke into very small pieces. The fragmentation is exactly the intended effect of this approach. The localized discharge caused a very small temperature rise and the cell voltage dropped briefly and recovered. After the indented area completed discharging, the rest of the cell was detached from it and kept its function. The leakage current was very small, indicating high resistance in the contact area. Cell heating was minimal even for the 100% SOC cells. Further indentation could not affect the surrounding areas and the cell thermal runaway risk was the lowest among all the batteries studied thus far.

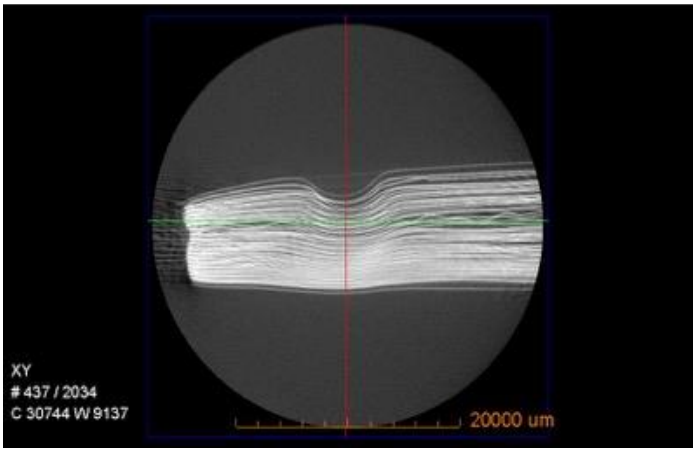

Figure 82. XCT image of 2 mm deep indentation of a MFCC NMC 811 cell (XY view).

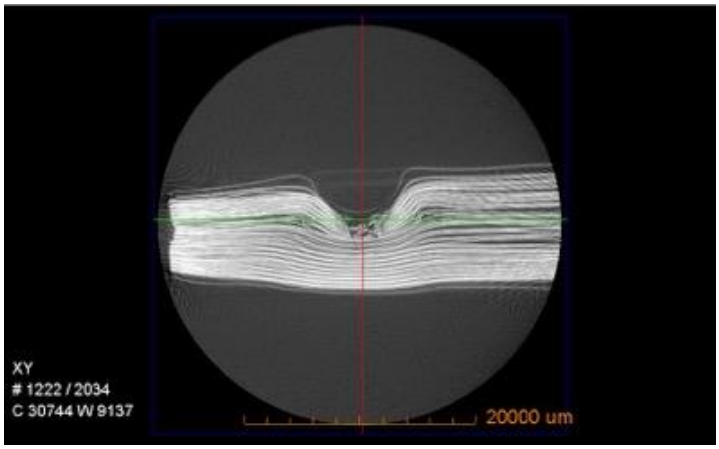

Figure 83. XCT image of 3 mm deep indentation of a MFCC NMC 811 cell (XY view).

In summary, indentation tests on 1 Ah NMC cells with slitted electrodes were performed. In theory, the slits should break into pieces when the indentation is deep enough, and the deformation area diameter is much larger compared to the slit spacing. In practice, the ideal deformation is very difficult to simulate experimentally. The slitted cells were shown to be more difficult (required higher force) go to trigger thermal runaway. The 5 Ah NMC 811 cells using MFCC were shown to be most successful in preventing thermal runaway. XCT results showed the electrodes broke into small pieces under the indenter resulting very localized short circuit and the discharge current was very small. The cell surface temperature never exceeded 30°C. The MFCC cells have the lowest thermal runaway severity score based on a new ORNL–Sandia analysis.

4.4.2 Nail Penetration Experiment

Nail penetration testing was performed on all groups of cells using the requested United States Advanced Battery Consortium LLC. Setup and procedures:

- Cells charged at C/10 constant current, constant voltage to a cutoff of C/50
- Cells placed in test fixture with thermal couple attached to approximate center of cell, voltage test leads attached
- Thermal, video, and data acquisition started (voltage and temperature)
- 3 mm nail driven into cell at 80 mm/s and left in cell for duration of test
- Sharp nails and blunt nails used for each type of cell

The test setup is shown in Figure 84.

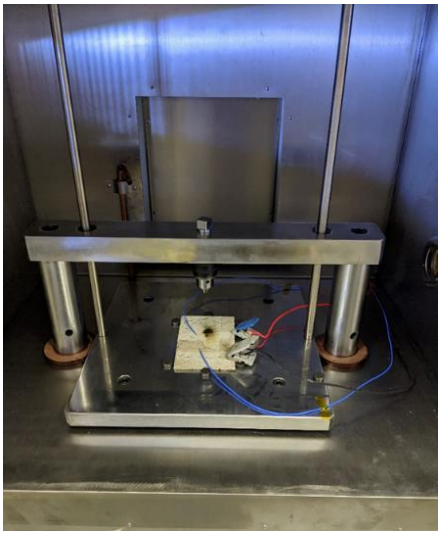

Figure 84. Nail penetration test setup.

Baseline cell performance

As shown in Figure 85, the typical control cell exhibited voltage drop close to zero after nail insertion. Temperatures on the surface of the cell increased slightly and then returned to ambient. Some cells exhibited some perturbation in the voltage, but the cell voltage then returned to >4 V. All seven cells achieved EUCAR 3 performance. Sharp vs. blunt nails did not display a significant difference. Of the seven control cells tested, four had no remaining capacity after nail insertion, and three had between 302 and 467 mAh of remaining capacity. Table 6 summarizes the information and Figure 86 shows the cell after the nail penetration test.

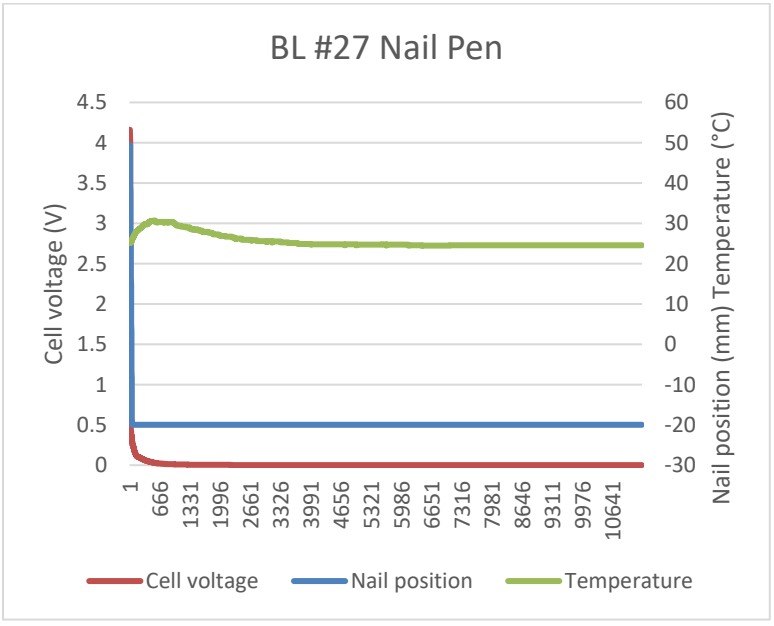

Figure 85. Typical nail penetration performance of BL cells.

Table 6. Nail penetration of BL cells

Test #	Cell	1000Hz Impedance (mohm)	Initial Capacity (mAh)	SOC (%)	Location	Nail	Result (EUCAR)	Video	LAD
1	TCF_BL_1Ah_#23_09292020	51.9	1004.12	100	Center	Sharp	3	raw data\r	430.9
2	TCF_BL_1Ah_#25_09292020	76.55	1047.27	100	Center	Sharp	3	raw data\r	302
3	TCF_BL_1Ah_#26_09292020	68.79	1050.11	100	Center	Sharp	3	raw data\r	N/A
4	TCF_BL_1Ah_#27_09292020	59.74	1030.63	100	Center	Blunt	3	raw data\r	N/A
5	TCF_BL_1Ah_#28_09292020	70.14	1003.15	100	Center	Blunt	3	raw data\r	467.3
6	TCF_BL_1Ah_#29_09292020	64.11	1028.69	100	Center	Blunt	3	raw data\r	N/A
7	TCF_BL_1Ah_#30_09292020	65.98	1032.02	100	Center	blunt	3	raw data\r	N/A

Figure 86. BL cell #12: top and bottom after testing (typical of all).

BL cell with slits performance

BL cells with slits exhibited a variety of responses to the nail penetration test. As shown in Figure 87, cell voltage had no response, immediate dropped to near zero, or had a perturbation when the nail was inserted. The temperature probe exhibited a similar range in responses, from very little increase to a slight increase to a large perturbation. This variety likely relates to the location of slits and nail penetration. All eight cells tested exhibiting EUCAR 3 performances. Sharp vs. blunt nails exhibited little difference. Three cells had no capacity after nail penetration. The remaining cells exhibited between 171 and 480 mAh of remaining capacity. Table 7 summarizes the information and Figure 88 shows the cell after the nail penetration test.

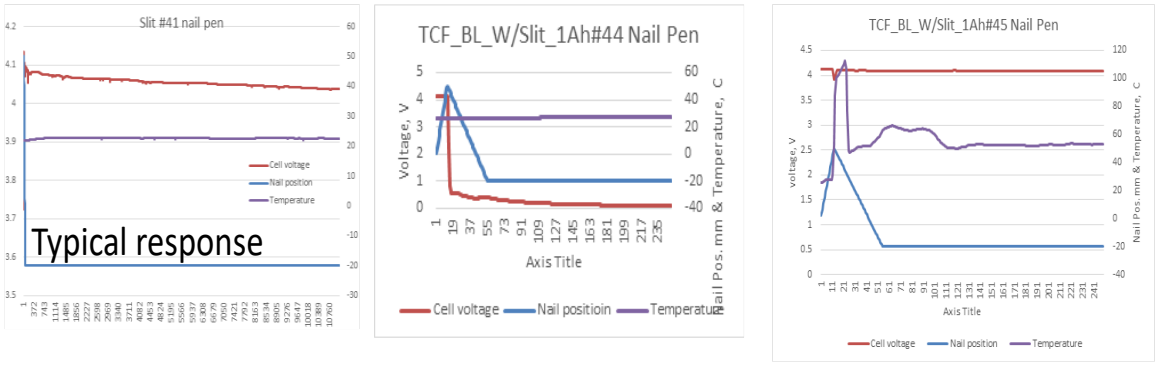

Figure 87. Nail penetration performance of BL cells with slits.

Table 7. Nail penetration of BL cells with slits

Test #	Cell	1000Hz Impedance (mohm)	Initial Capacity (mAh)	SOC (%)	Location	Nail	Result (EUCAR)	Video	LAD
1	TCF_BL_W/Slit_1Ah_#41_09292020	51.12	1051.33	100	Center Tile	Sharp	3	raw data\r	171.6
2	TCF_BL_W/Slit_1Ah_#42_09292020	53.82	1019.2	100	Center Tile	Sharp	3	raw data\r	346.7
3	TCF_BL_W/Slit_1Ah_#43_09292020	56.68	1076.84	100	Center Tile	Blunt	3	raw data\r	360.5
4	TCF_BL_W/Slit_1Ah_#44_10012020	61.57	1074.32	100	Center Tile	Blunt	3	raw data\r	N/A
5	TCF_BL_W/Slit_1Ah_#45_10012020	50.58	1066.61	100	Slit Junction	Sharp	3	raw data\r	479.8
6	TCF_BL_W/Slit_1Ah_#46_10012020	71.38	1079.4	100	Slit Junction	Sharp	3	raw data\r	N/A
7	TCF_BL_W/Slit_1Ah_#47_10012020	71.1	1047.24	100	Slit Junction	Blunt	3	raw data\r	N/A
8	TCF_BL_W/Slit_1Ah_#48_10012020	56.26	1076.51	100	Slit Junction	Blunt	3	raw data\r	411.4

Figure 88. BL cell #45 with slits: top and bottom after testing (typical of all).

MP cell performance

The MP cells exhibited very little detectible activity upon nail insertion. As shown in Figure 89, all cells achieved EUCAR 3 performance. Sharp vs. blunt nails exhibited little difference. All cells exhibited capacity after damage between 206 and 492 mAh. Table 8 summarizes the information and Figure 90 shows the cell after the nail penetration test.

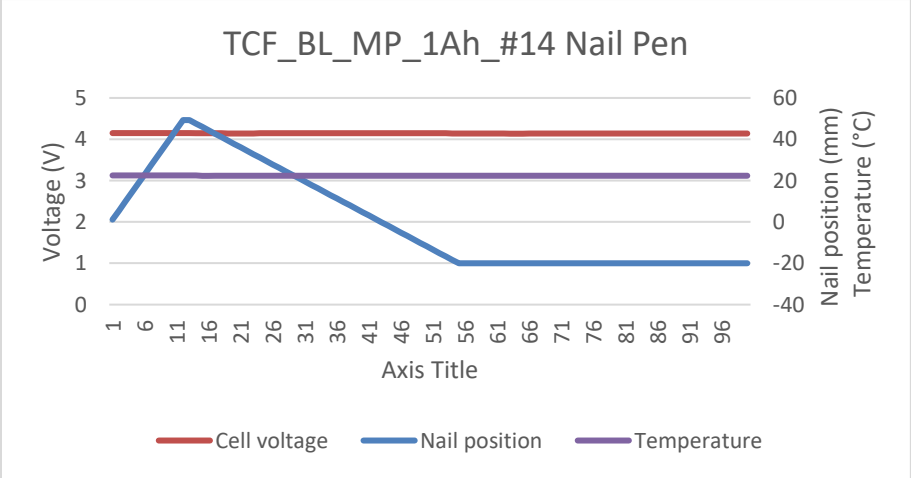

Figure 89. MP cell #14 voltage and temperature (typical of all).

Table 8. Nail penetration of MP cells

Test #	Cell	1000Hz Impedance (mohm)	Initial Capacity (mAh)	SOC (%)	Location	Nail	Result (EUCAR)	Video	LAD (mAh)
1	TCF_BL_MP_1Ah_#10_12152020	201.6	1018.83	100	Center	Sharp	3.00	raw data\t	205.5
2	TCF_BL_MP_1Ah_#11_12152020	139.63	1036.15	100	Center	Sharp	3.00	raw data\t	422
3	TCF_BL_MP_1Ah_#12_12152020	259.54	1024.7	100	Center	Sharp	3.00	raw data\t	414.5
4	TCF_BL_MP_1Ah_#13_12152020	221.44	997.645	100	Center	Blunt	3.00	raw data\t	492.4
5	TCF_BL_MP_1Ah_#14_12152020	255.64	988.39	100	Center	Blunt	3.00	raw data\t	424.6
6	TCF_BL_MP_1Ah_#15_12302020	162.55	1024.89	100	Center	Blunt	3.00	raw data\t	403.7

Figure 90. MP cell #14: top and bottom after testing (typical of all).

MP cells with slits performance

The MP cells with slits all exhibited very little detectible reaction to the nail penetration as shown in Figure 91. All cells displayed EUCAR 3 performance. Sharp vs. blunt exhibited little difference. All cells had capacity after damage ranging from 92 to 411 mAh of capacity after nail penetration. Table 9 summarizes the information and Figure 92 shows the images of post nail penetration test.

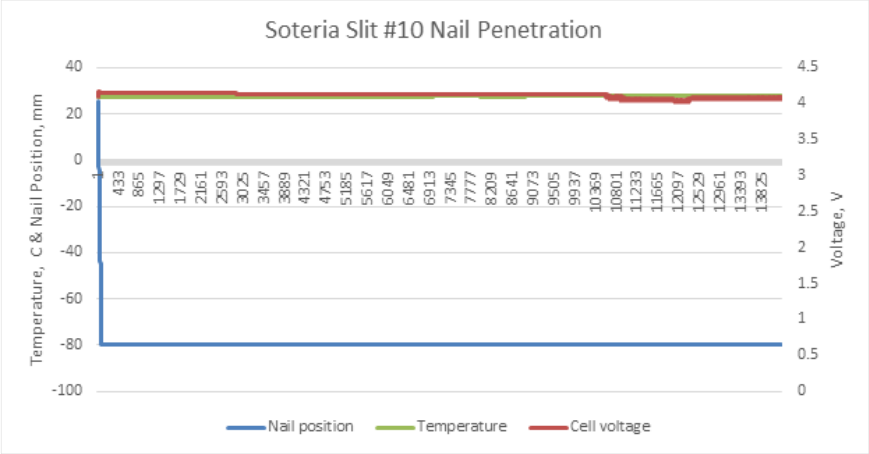

Figure 91. MP cell #10 with slits voltage and temperature (typical of all).

Table 9. Nail penetration of MP cells with slits

Test #	Cell	1000Hz Impedance (mohm)	Initial Capacity (mAh)	SOC (%)	Location	Nail	Result (EUCAR)	Video	LAD (mAh)
1	TCF_BL_MP_SL_1Ah_#10_12302020	220.8	925	100	Center	Sharp	3	raw data\r	454.4
2	TCF_BL_MP_SL_1Ah_#11_12302020	262.3	964	100	Center	Sharp	3	raw data\r	410.9
3	TCF_BL_MP_SL_1Ah_#12_12302020	121.83	908.9	100	Center	Sharp	3	raw data\r	404.6
4	TCF_BL_MP_SL_1Ah_#13_12302020								
5	TCF_BL_MP_SL_1Ah_#14_12302020								
6	TCF_BL_MP_SL_1Ah_#15_12302020								
7	TCF_BL_MP_SL_1Ah_#17_12302020	7725	904.9	100	Center	Blunt	3	raw data\r	19.0
8	TCF_BL_MP_SL_1Ah_#24_06142021	460.7	930.1	100	Center	Blunt	3	raw data\r	100.0
9	TCF_BL_MP_SL_1Ah_#25_06142021	431.1	910.6	100	Center	Blunt	3	raw data\r	92.4

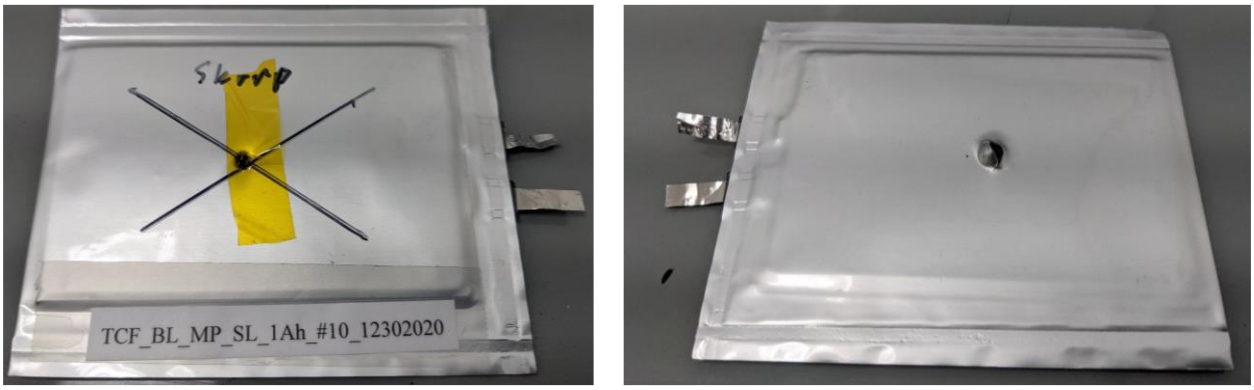

Figure 92. MP cell #10 with slits: top and bottom after testing (typical of all).

In summary, all cells tested exhibited EUCAR 3 level of performance in response to both blunt and sharp nail penetration tests. Differences between the groups are shown in graphs of voltage and temperature, and in the life performance after damage capacity testing. As a general trend, the BL cells without slits exhibited the worst performance, followed by the BL cells with slits, the MP cells with slits, and finally the MP cells without slits.

5. SUBJECT INVENTIONS

One research license has been established from US Patent 10,374,234 B2 and 9,847, 531 B2 through a license agreement number PLA-1967. Three papers will be developed from the project, including one under review and two under preparation.

6. COMMERCIALIZATION POSSIBILITIES

The LIB market is expected to increase from $21.95 billion in 2020 to $154.90 billion in 2028, primarily driven by the movement into electric mobility [13]. Based on announced gigafactories, capacity for LIB manufacturing is expected to move past 7 TWh by 2031, with nearly 120 companies announcing gigafactories. Nine companies (CATL, Panasonic, BYD, Envision AESC, LG Energy Solution, SK Innovation, and Samsung SDI) make up more than half of this capacity [14]. Advancements in battery technology are primarily driven by performance (i.e., long cycle life, fast charge capability, high energy density). Typically, improvements to battery performance come with the trade-off of decreased safety, and there is increasing attention around battery safety because of public battery fires and costly recalls. Some notable incidents include the $2 billion recall for the Chevy Bolt [15], the grid storage fire in Chandler, Arizona [16], and the New York City Fire Department's exploration into banning electric bikes from New York City [17]. Most of the batteries involved in these incidents had passed the current safety requirements, prompting the push to improve safety standards.

Along with the goal to improve safety standards, technologies such as those discussed in this report are becoming increasingly popular. Soteria, with its MFCC, has a goal to achieve 25% market penetration by 2030, yielding a potential >$800 million in annual royalties. This is based on the study of other battery technologies that have taken a licensing model, such as Celgard's ceramic-coated separator and 3M's NMC powder. Soteria continually aims to understand customer needs in a variety of markets. Through these customer studies, Soteria has identified initial target markets that have a shorter design time to commercialization. These initial markets include drones, low-speed electric vehicles, power tools, and electric bikes and sports. The first of these markets is the drone industry. This market is expected to reach 9 GWh by 2025 at a high value of approximately $800/kWh, or $7.2 billion. When drones fall, damage to the battery cells can cause them to catch fire in residential or industrial areas, or over forest or crop lands. Drone batteries experience significant use, and drone fliers are very conscious of safety. Low-speed electric vehicles include a variety of vehicles, including golf carts, forklifts, and electric two- and three-wheelers. Uses include carrying passengers in residential areas and cargo in chemical factories and mines. Many electric vehicles enter critical environments, some spend long periods on chargers unattended, and some are significantly misused. The market size is expected to be 25 GWh by 2025 as this market transitions from lead acid to lithium ion. Power tools require high power, are used in all sorts of environments, and experience significant mechanical use. Power tools include lawn and garden tools, such as chainsaws and riding lawn mowers. The market size is expected to be 9 GWh in 2025, but this may be an underestimate as the larger lawn and garden device segment is growing rapidly. Electronic bikes and sports experience significant market growth during the COVID-19 pandemic, more than tripling in size in the United States. Electronic bikes include scooters, road bikes, and mountain bikes. Several scooter and bike rental companies have had to recall all the electric bikes in a given city because of fires. The batteries experience significant mechanical abuse and are used in many different environments. The market size is expected to be 22 GWh in 2025, with the fastest growth occurring in Europe and the United States.

There are other opportunities in which safe technology is ready for but technical development is still lacking. These include energy storage systems (65 GWh in 2025), electric vehicles (3 TWh in 2030), electric air mobility (difficult to determine), and consumer electronics (34 GWh in 2025).

7. PLANS FOR FUTURE COLLABORATION

ORNL and Soteria have built on the effort from this CRADA and extended the application of metallized polymer films to a fast charging application. The two parties have won a joint proposal entitled "Multilayer Electrodes with Metallized Polymer Current Collector for High-Energy LIBs with Extreme-Fast-Charging Capability," which was funded by the Advanced Manufacturing Office in 2021. The project started in 2022. Additionally, the two parties submitted a concept paper to the Advanced Research Project Agency-Energy in 2022. Other opportunities for further collaboration are also being explored. Options include calls from the Advanced Research Project Agency-Energy, Advanced Manufacturing Office, Vehicle Technologies Office, Small Business Innovation Research, Small Business Technology Transfer, and more.

8. CONCLUSIONS

Electrodes were successfully fabricated with metallized polymer films as current collectors. Various slit patterns were designed. Temperature distribution was evaluated via simulation. Four types of pouch cells with different collectors and with and without slits were assembled. Comparable cycle performance was observed. The rate performance was also almost identical at a low C-rate (i.e., C/2). The use of slits lowered the rate performance at high rates. Nail penetration and indentation tests demonstrated improved safety features from cells with metallized polymer films.

9. REFERENCES

[1] Naguib, M., Allu, S., Simunovic, S., Li, J. L., Wang, H., and Dudney, N. J., 2018, "Limiting Internal Short-Circuit Damage by Electrode Partition for Impact-Tolerant Li-Ion Batteries," Joule, 2(1), pp. 155-167.

[2] Klein, M., Hadrboletz, A., Weiss, B., and Khatibi, G., 2001, "The 'size effect' on the stress-strain, fatigue and fracture properties of thin metallic foils," Materials Science and Engineering a-Structural Materials Properties Microstructure and Processing, 319, pp. 924-928.

[3] Wang, H. W., Kang, Y. L., Zhang, Z. F., and Qin, Q. H., 2003, "Size effect on the fracture toughness of metallic foil," International Journal of Fracture, 123(3-4), pp. 177-185.

[4] Merchant, H. D., Khatibi, G., and Weiss, B., 2004, "Elastic and elastoplastic response of thin copper foil," Journal of Materials Science, 39(13), pp. 4157-4170.

[5] Wang, H. W., and Ji, H. W., 2006, "Size effect and microscopic experimental analysis of copper foils in fracture," pp. 263.

[6] Suzuki, K., Matsuki, Y., Masaki, K., Sato, M., and Kuroda, M., 2009, "Tensile and microbend tests of pure aluminum foils with different thicknesses," Materials Science and Engineering a-Structural Materials Properties Microstructure and Processing, 513-14, pp. 77-82.

[7] Andreasson, E., Kao-Walter, S., and Stahle, P., 2014, "Micro-mechanisms of a laminated packaging material during fracture," Engineering Fracture Mechanics, 127, pp. 313-326.

[8] Bonatti, C., and Mohr, D., 2016, "Anisotropic viscoplasticity and fracture of fine grained metallic aluminum foil used in Li-ion batteries," Materials Science and Engineering a-Structural Materials Properties Microstructure and Processing, 654, pp. 329-343.

[9] Mohanty, D. P., Rao, V. L., Das, S. L., and Ghatak, A., 2017, "Polygonal deformation of a metallic foil subjected to impact by an axisymmetric indenter," Journal of Adhesion Science and Technology, 31(15), pp. 1647-1657.

[10] Belytschko, T., Liu, W., and Moran, B., 2000, Nonlinear Finite Elements for Continua and Structures, Wiley New York.

[11] LSTC, 2014, LS-DYNA Keyword User's Manual, Livermore Software Technology Corporation.

[12] Allu, S., Kalnaus, S., Simunovic, S., Nanda, J., Turner, J.A. and Pannala, S., 2016. A three-dimensional meso-macroscopic model for Li-ion intercalation batteries. *Journal of Power Sources*, *325*, pp.42-50.

[13] Electric Vehicle Battery Market Size to Grow Worth USD 154.90 Billion (Global Newswire)

[14] Benchmark: Li-Ion Battery 2031 Pipeline Blows Past 7TWh (Green Car Congress)

[15] The Enormous Cost of the Bolt EV Recall is Falling on LG (Popular Science)

[16] 4MW of AES' Lithium Batteries Burn in Chandler, Arizona (Data Center)

[17] NYC May Ban E-Bikes in Public Housing Following a Spate of Fires (Canary Media)